Please note that this is an author-produced PDF of an article accepted for publication following peer review. The definitive publisher-authenticated version is available on the publisher Web site

Applied and Environmental Microbiology
May 2008 ; Volume 74 (10) : Pages 3198-3215
http://dx.doi.org/10.1128/AEM.01751-07
© 2008, American Society for Microbiology. All Rights Reserved.

Archimer
Archive Institutionnelle de l'Ifremer
http://www.ifremer.fr/docelec/

Biogeochemistry and Community Composition of Iron- and Sulfur-Precipitating Microbial Mats at the Chefren Mud Volcano (Nile Deep Sea Fan, Eastern Mediterranean)

Enoma O. Omoregie[1, 2, *], Vincent Mastalerz[3], Gert de Lange[3], Kristina L. Straub[4, 8], Andreas Kappler[4], Hans Røy[1], Alina Stadnitskaia[5], Jean-Paul Foucher[6] and Antje Boetius[1, 2, 7]

[1] Max Planck Institute for Marine Microbiology, Bremen, Germany
[2] Jacobs University, Bremen, Germany
[3] Department of Earth Sciences, Utrecht University, Utrecht, The Netherlands
[4] Center for Applied Geosciences, Eberhard Karls University, Tübingen, Germany
[5] Royal Netherlands Institute for Sea Research (NIOZ), Texel, The Netherlands
[6] Department of Marine Geosciences, IFREMER Centre de Brest, Plouzané Cedex, France
[7] Alfred Wegener Institute for Polar and Marine Research, Bremerhaven, Germany
[8] Present address: Department of Biogeochemistry, Vienna University, Vienna, Austria.

*: Corresponding author : Enoma O. Omoregie, Phone: (44) 161-275-5668, Fax: (44) 0161-306-9361, email address : enoma.omoregie@manchester.ac.uk

Abstract:

In this study we determined the composition and biogeochemistry of novel, brightly colored, white and orange microbial mats at the surface of a brine seep at the outer rim of the Chefren mud volcano. These mats were interspersed with one another, but their underlying sediment biogeochemistries differed considerably. Microscopy revealed that the white mats were granules composed of elemental S filaments, similar to those produced by the sulfide-oxidizing epsilonproteobacterium "*Candidatus* Arcobacter sulfidicus." Fluorescence in situ hybridization indicated that microorganisms targeted by a "*Ca*. Arcobacter sulfidicus"-specific oligonucleotide probe constituted up to 24% of the total the cells within these mats. Several 16S rRNA gene sequences from organisms closely related to "*Ca*. Arcobacter sulfidicus" were identified. In contrast, the orange mat consisted mostly of bright orange flakes composed of empty Fe(III) (hydr)oxide-coated microbial sheaths, similar to those produced by the neutrophilic Fe(II)-oxidizing betaproteobacterium *Leptothrix ochracea*. None of the 16S rRNA gene sequences obtained from these samples were closely related to sequences of known neutrophilic aerobic Fe(II)-oxidizing bacteria. The sediments below both types of mats showed relatively high sulfate reduction rates (300 nmol·cm^{-3}·day^{-1}) partially fueled by the anaerobic oxidation of methane (10 to 20 nmol·cm^{-3}·day^{-1}). Free sulfide produced below the white mat was depleted by sulfide oxidation within the mat itself. Below the orange mat free Fe(II) reached the surface layer and was depleted in part by microbial Fe(II) oxidation. Both mats and the sediments underneath them hosted very diverse microbial communities and contained mineral precipitates, most likely due to differences in fluid flow patterns.

Introduction

Submarine mud volcanoes are geological structures formed by episodic eruption of gases and muds from deep subsurface reservoirs. Some mud volcanoes continuously expel reduced muds, fluids and gases to the ocean, supplying chemical energy to cold seep organisms, such as dense mats of giant sulfur-oxidizing bacteria, siboglinid tubeworms, and a variety of bivalves (74). Active mud volcanoes with such cold seep ecosystems are known from the Central Mediterranean Ridge (15, 64, 95), the Central American continental margin (52), the Gulf of Cadiz (60) and the Barents Sea (61). In the Eastern Mediterranean, active mud volcanism associated with diverse ecosystems have recently been detected on the Nile Deep Sea Fan (15, 42, 49, 65).

At mud volcanoes as well as many other cold seeps, methane and sometimes higher hydrocarbons are transported upwards with rising fluids and muds, and can escape to the hydrosphere in the form of gas or oil bubbles (53, 61, 71). Anaerobic hydrocarbon degradation forms the basis of a steep sequence of biogeochemical processes connecting the carbon and sulfur cycles at these sites (1, 72). When hydrocarbons reach the sulfate penetrated sediment zones, they are utilized by sulfate reducing bacteria (SRB) as energy and carbon sources. The products of sulfate respiration with methane and higher hydrocarbons are sulfide and bicarbonate (1, 8, 30). Hence, hydrocarbon seepage is generally associated with high sulfide fluxes (61, 84). At methane seeps, most of the sulfide is produced via the anaerobic oxidation of methane (AOM) mediated by anaerobic methanotrophic archaea (ANME; (22), and references therein). However, several oily cold seep systems (30, 60) including some in the Eastern Mediterranean (65) have been

discovered where anaerobic oxidation of higher hydrocarbons coupled to sulfate reduction was the dominant sulfide source.

Sulfide is central to biogeochemical cycling in marine sediments as an energy-rich microbial substrate and the principle product of one of the most quantitatively important respiratory processes in ocean sediments, namely sulfate reduction (34). Sulfide reacts spontaneously with Fe(III) and Fe(II) (83), Mn(II) and Mn(IV) (10), and is used as an electron donor for a variety of aerobic and anaerobic sulfide-oxidizing microorganisms. Well-known marine sulfide-oxidizing organisms include the giant vacuolated γ-proteobacteria, such as *Beggiatoa* and *Thiomargarita* spp., which use oxygen or nitrate for respiration and often form dense mats above hydrocarbon seeps (8, 31, 61, 63). Other types of sulfide-oxidizing bacteria mostly known from hydrothermal vent systems, but also found sporadically at cold seep systems, belong to the *Epsilonproteobacteria* (11). Little is known about the nature and functioning of other types of bacteria and archaea, which appear commonly associated with cold seep ecosystems such as the crenarchaeotal groups MBGB and MBG1 (37, 38, 54).

Here we report on our investigation of the biogeochemistry and microbial community structure of two types of closely associated bacterial mats. These mats were discovered during a dive with the submersible *Nautile* (IFREMER) to a brine-impacted cold seep at the bottom of the Chefren mud volcano located in a large caldera of the western Nile Deep Sea Fan (Menes Caldera). Similar types of mats have been seen at hydrothermal vents (17, 77, 80), but to date have not been described in association with cold seeps. In this study we combined microscopic, biogeochemical and molecular analyses to identify the underlying factors that cause the formation of these two distinct

mat systems. This work was part of the ESF EUROCORES EUROMARGIN project MEDIFLUX, which is an integrated study of fluid and gas seepage through the seabed of the Nile Deep Sea Fan.

Materials and Methods

Sampling location. The Chefren mud volcano of the MENES Caldera was discovered by bathymetry surveys of the Western Nile Deep Sea Fan during the “FANIL” expedition in 2000 (50). Its sediments were sampled for the first time in the “NAUTINIL” expedition (this study) with the RV *L’Atalante* and submersible *Nautile* (IFREMER) in September 2003. The Menes Caldera (Fig. 1A) is a 8 km diameter circular depression of approximately 50-100 m depth, located at about 3,000 m water depth in the western province of the Nile Deep Sea Fan. This caldera hosts three mud volcanoes, Chefren, Cheops and Mykerinos (Fig. 1B). Chefren is about 500 m in diameter and rises to about 60 m above the bottom of the Caldera (3020 m) (Fig. 1C). At the time of sampling the center of this mud volcano was filled by a large and deep brine and mud lake. For a more detailed description of the Menes Caldera and associated structures, see Huguen et al., (23)

Sampling. Sediment samples were recovered from the orange and white mats by the submersible *Nautile* (Fig. 2A,B; N 32° 06.74’, E 028° 10.35’, 3,024 m water depth). The samples were collected using 6 cm diameter push cores. Two push cores were taken from the orange mat (NL18PC1(8); NL18PC2(7); Fig. 2E) and 2 from the white mat above

black sediments (NL18PC3(5); NL18PC4(6); Fig. 2D), as well as 2 blade cores (NL18BC1(L3), NLBC2(L7)) from the nearby sediments. Upon returning to the RV *L'Atalante*, cores were immediately taken to the cold room and sub-sampled by 1 cm diameter sub-cores for further analyses as described below. Cores NL18PC3(5) and NL18PC1(8) were used for microbiological analyses as well as rate measurements, whereas cores NL18PC4(6) and NL18PC2(7) were used for geochemical analyses. Due to the exploratory nature of the expedition, the sampling material was limited to one dive.

Methane concentration. Sub-cores were sectioned and preserved with 2.5% NaOH in rubber sealed glass vials. Methane concentrations were measured by injecting 100 µl of head space in a Hewlett Packard 5890A gas chromatograph.

Methane oxidation rate determinations. Methane oxidation rates were measured using $^{14}CH_4$ gas, based on previously described methods (26, 84). Subcores were injected with 10 µl of $^{14}CH_4$ (2.5 kBq total, dissolved in ddH_2O) and incubated for 24 hr in the dark at *in situ* temperature of 14°C. Following the incubations the cores were sectioned and fixed with 2.5% NaOH. Further processing was done according to Treude et al. (84). Rates were determined using the equation below, where $^{14}CO_2$ = activity of CO_2 produced, $^{14}CH_4$= activity of residual injected $^{14}CH_4$, $[CH_4]$ = CH_4 concentration, *V*= sediment volume and *t*= time.

$$\text{AOM rate} = (^{14}CO_2/(^{14}CO_2 + {}^{14}CH_4)) * [CH_4] / V / t$$

Sulfate reduction rate determination. Sulfate reduction rate measurements were made using $^{35}SO_4^{-2}$ based on previously described methods (29). Subcores were injected with 5 µl $^{35}SO_4^{-2}$ (100 kBq total, dissolved in ddH_2O) and incubated for 24 hours at *in situ* temperature in the dark. Following the incubations, the sediment was sectioned and placed in a polypropylene tube containing 20% zinc acetate. Further processing was done according to Kallmeyer et al (32). Rates were calculated according to the equation below, where $TRIS^{35}S$ = activity of total reduced inorganic sulfur, $^{35}SO_4^{2-}$ = activity of residual $^{35}SO_4^{-2}$ tracer, $[SO_4^{-2}]$ = SO_4^{-2} concentration within the sample, V = sediment volume, and t = time.

$$\text{SR rate} = (TRI^{35}S/(TRI^{35}S + {}^{35}SO_4^{-2})) * [SO_4^{-2}] / V / t$$

Geochemical measurements. For sulfide analysis, 10 µl of 0.1 N NaOH was added to 2 ml pore water sub-samples. Sub-samples were measured on board using a TRAACS800 continuous flow analyzer, applying colorimetric methods after Grasshoff et al. 1983 (21). Pore-water major element analyses was conducted with inductively coupled plasma atomic emission spectroscopy (ICP-AES), 2 ml sub-samples were acidified by adding 100 µl of suprapur HNO_3 acid (1 M), bubbled to remove sulfide, and stored in the dark at 4°C. Sulfate concentrations were measured as S. The standard deviation for all measurements was 3% or better. The geochemical composition of the solid phase was also determined by ICP-AES after total dissolution of sediments in an acid mixture of $HClO_4$, HNO_3, and HF (67). Organic carbon content was determined according to the method described by Van Santvoort et al., (89). International and in-house standards and duplicates were processed to monitor precision and accuracy. Note, very little pore water

was recovered from 7-9cm sample from the orange mat; therefore there is likely a high error associated with values from that sample.

Light and epifluorescence microscopy. Sediment sections were preserved in 2% formalin and artificial seawater for Acridine Orange (AO) staining as well as for light microscopy. Samples for Fluorescence In Situ Hybridization (FISH) were initially fixed in a 2% formalin and seawater solution, washed several times with PBS and finally stored in a PBS/ethanol solution (1:1). Specific groups of *Bacteria* and *Archaea* were quantified using CARD-FISH (Catalyzed Reporter Deposition) except for the quantification of ANME-2 and aerobic methanotrophic bacteria (Mγ705 probe, ref 16) for which monolabeled FISH probes were used because no result was obtained with CARD-FISH probes. AO staining (7), FISH (76) and CARD-FISH (25) were all performed according to previously described methods. All FISH and CARD-FISH slides were counter-stained with DAPI (4´,6´- diamidino-2-phenylindole). At least 30 grids were counted randomly from each slide for AO, FISH and CARD-FISH counts. Probe hybridization details are given in Table 1. Cell numbers within conspicuous ANME-SRB aggregates were estimated using a semi-direct method (8). All aggregates and cells were assumed to be spherical. The average cell volume was estimated to be 0.065 μm^3. The volume of an average aggregate (82 μm^3) was divided by the cell volume, and a ratio of 1:1 archaeal to bacterial cells was used to calculate bacterial and archaeal cell numbers within the consortium.

SEM-EDX. Formalin-fixed samples were analyzed with the scanning electron microscope LEO 1550VP equipped with an inlense detector. Element analysis was performed with an INCA Energy 300 System equipped with a Si(Li) detector.

16S rRNA gene construction and phylogenetic analysis. Sectioned sediment samples were frozen at -20°C until processing. 16S rRNA gene, archaeal and bacterial libraries were created after Niemann et al. (60). Briefly, total community DNA was extracted from sediment sections and orange flakes using the FastDNA spin kit for soil (Q-Biogene, Irvine, California, USA). Total DNA was extracted from formalin preserved white granules using Chelex-100 resin. Granules were boiled at 100°C in presence of Chelex-100 resin, the beads were allowed to settle and the supernatant was used for PCR. The 16S rRNA gene was amplified from archaea using the primers ARCH20F (51) and Uni1392R (40), and from bacteria using GM3F (55) and GM4R (33). Amplification products were cloned, and purified plasmid sequenced using an ABI 3100 genetic analyzer. Plasmids were sequenced initially in one direction (approximately 0.6 kb). Sequences were manually inspected, and poor quality sequences removed from further analysis. Sequences were also screened for chimeras using the program Mallard (4). Anomalous sequences were then further investigated using BLAST and the program Pintail (3). Sequences with genuine chimeras were then excluded from further analyses. Selected clones were then sequenced fully (approximately 1.5 kb) and used for subsequent phylogenetic analysis within the ARB (46) software package. Statistical analysis on 16S rRNA gene libraries was performed using the s-libshuff program by Schloss et al. (73). Distances matrices calculated in ARB using the Neighbor-joining tool

were used for s-libshuff. Sequences from this study were deposited within the GenBank database and are accessible under the following accession numbers: EF687138-EF687656 and EF688595.

Fluid flow models. Mass transfer models including fluid flow and molecular diffusion were created in the modeling suite Comsol-Multiphysics and calibrated against the measured Cl^- concentration. As Cl^- can be regarded as non reactive, the mass balance is governed by diffusion and advection according to the equation below, where Cl^- = pore water Cl^- concentration, z = vertical distance, φ= porosity, Ds = diffusion coefficient for Cl^- in the pore space and v = the vertical velocity.

$$o = \varphi * Ds * d^2C/dz^2 - v\,\varphi\, dC/dz$$

Diffusion coefficients were corrected for tortuosity via the interpolated porosity in each depth following the procedure from Iversen and Jørgensen (27). Concentrations at the surface were set to the Cl^- concentration measured in the bottom water of the push cores and the concentration at the lower boundary of the modeled regime (1 m) was set to the concentration measured below 15 cm (below white mat) or 17 cm (below orange mat) in both cores. This leaves the pore water flow as the only unknown, which can be estimated by numerically finding the best fit to the measured Cl^- profiles. Each steady state calculation was followed by 10 hours of stagnation to include the time the sediment was contained in the core liner before sectioning.

Results

Visual observations. White mats and orange mats were located at a small brine seep, on a steep slope at the bottom of a small mound adjourning the northwestern rim of the Chefren mud volcano (Fig. 1C), at 3,020 m water depth. The mats showed a patchy distribution and covered about 25 m^2 (Fig. 2A,B). Shimmering brine fluid flowed downwards from black sediments above the white mats (Fig. 2B). Associated with the orange patches at this site, but also at other areas of Chefren we observed many crabs feeding on the sediments, which were populated by small worm tubes sticking out 1-2 cm above the sediment. The surfaces of the cores recovered from the white mat were composed of thick white cotton ball like precipitates that resembled filamentous S aggregates (Fig. 2C), which have previously been observed at hydrothermal vents (81). Polychaete larvae (Fig. 2C) were observed crawling through the white mats as well as through the surface of the core. The surfaces of the cores from orange mat were composed of a thick layer of fluffy yellow material, as well as flaky, bright orange particles, resembling Fe(III)-(hydr)oxides (Fig. 2D). Similar to the core from the white mat, polychaete larvae were also associated with the orange mat.

We followed the orange and white mat structure to the SW along the same depth contour for about 50 m. Irregular patches of orange mat occurred within a band of about 2 m in diameter, and also in association with the edge of the brine lake in the center of the Chefren (Fig. 2E). When using the manipulator arm of *Nautile* to dig into the orange patches, we could observe that the subsurface sediments were dark grey to blackish while the surrounding seafloor was of light brown-beige color, typical for pelagic sediments in

252 the deep Eastern Mediterranean. No trace of gas ebullition was observed upon
253 disturbance of the seafloor. Wide areas of the brine lakes located at the top of Chefren
254 and Cheops mud volcanoes were covered with white mats (Fig. 2F) similar to those
255 observed on the sediments.
256
257 **Microscopy.** Examination of the granules recovered from the surface of the white mat
258 (Fig. 3A), revealed the presence of tufts of thin filaments (Fig. 3B), morphologically
259 similar to those produced by the *Epsilonproteobacterium* "*Candidatus* A. sulfidicus" (80,
260 81). Scanning electron microscopy (SEM) coupled to energy dispersive X-ray analysis
261 (EDX) revealed these tufts to be characterized by high amounts of Fe and S (Fig. 3C).
262 Framboidal pyrite grains (not shown) were also detected within these granules.
263 Fluorescence in Situ Hybridization (FISH) with probe Arc94 (Fig. 3D), which targets
264 "*Ca* A. sulfidicus" and related species indicated that this group of organisms constituted
265 up to 25% of the total cells within the white granules and in the underlying black
266 sediment (Table 2). However, several morphologies (e.g. filamentous, coccoid) of cells,
267 which hybridized with the probe were observed, some of which were not the typical
268 crescent shaped "*Ca.* A. sulfidicus" cells.
269 Microscopic examination of flakes recovered from the surface of the orange mat
270 (Fig. 2D and Fig 3E) revealed numerous microbial sheaths of assorted sizes (Fig. 3F, G),
271 similar to those produced by or attributed to the neutrophilic Fe(II)-oxidizing bacterium
272 *Leptothrix ochracea* (17, 18, 87). EDX revealed that many of these sheaths were
273 associated with high amounts of Fe and O, indicating encrustation by Fe(III)-
274 (hydr)oxides. Most sheaths were sheared and empty (Fig. 3G). DAPI and AODC staining

both showed that only very few sheaths (< 1%) were populated with cells. FISH with EUB I-III revealed that these sheaths contained bacteria some of which could be targeted by Mγ705 probe (Fig. 3H) for type I methanotrophs, but not by domain specific probes for *Alpha-*, *Beta-* or *Gammaproteobacteria*. Two morphotypes of sheathed bacteria were targeted by the Mγ705 probe; one with rectangular cells similar to *Clonothrix fusca* (90), and the other square cells similar to *Crenothrix polyspora* (78). These two morphotypes often appeared bundled together.

Fluid flow model. The orange mats had a shallow Cl- gradient indicative of relatively low fluid flow. Hence, the 10 hours stagnation of the flow in the core liners had little effect on the shape of the profile and the upward fluid flow velocity could be calculated with good accuracy to 0.6 m a^{-1} (Fig. 4B). The white mats were associated with a much steeper Cl^- gradient indicating higher fluid flow velocities. The relaxation of the gradient during the 10 hour recovery caused the maximum velocity to be uncertain, but the minimum upward fluid flow under the white mat was estimated to be 15 m a^{-1} (Fig. 4A).

Biogeochemistry. Close to the white mat, Cl^- and Na^+ concentrations were up to 1.8 times higher than in the bottom water (water overlying the sediment in the core), indicating upward brine flow through the sediments (Table 3). Pore water sulfate concentrations under the white mat (Fig. 5A) were close to seawater values at the surface and decreased to about 19 mM immediately below the surface, possibly reflecting sulfate concentrations in the upward seeping fluids. Sulfate reduction (SR) rates (Fig. 5A) were highest in the top 4 cm (300 nmol*cm^{-3}*d^{-1}) and 70-fold higher than anaerobic oxidation

298 of methane (AOM) rates (Fig 5B). Methane concentrations (Fig. 5B) ranged from 0.1
299 mM at the top of the core to about 0.05 mM at the bottom. AOM rates were low
300 throughout the top 12 cm of sediment, with a maximum (10 nmol*cm^{-3}*d^{-1}) at 2 - 4 cm
301 sediment depth (Fig. 5B). Sulfide concentrations (Fig. 5C) approached 1 mM within the
302 zone of highest SR activity. Concurrently, Fe(II) (Fig. 5C) was depleted to <0.01 mM
303 above 5 cm, but increased to about 0.2 mM below this zone. These gradients match visual
304 characteristics of the core, namely the precipitation of Fe(II) with sulfide in the black,
305 highly reduced sediment horizon of up to 6 cm below the white mat (Fig. 5D). In this
306 layer, the Fe and S content (Table 3) of the solid phase was several times higher than in
307 underlying sediments, indicating a high content of FeS and pyrite.
308 Below the orange mat, sulfate concentrations decreased from 28 mM at the
309 surface to about 5 mM at 8 cm sediment depth (Fig. 5E). Cl^- and Na^- concentrations
310 indicated that these sediments were also brine impacted, although to a lesser extent than
311 the sediment underlying the white mat (Table 3). Maximum SR rates (400 nmol*cm^{-3}*d^-
312 ^{1}) (Fig. 5E) were located between 6 - 10 cm. This coincided with blackish, reduced
313 sediment similar to that observed directly beneath the white mat. A second SR maximum
314 (150 nmol*cm^{-3}*d^{-1}) was detected at 0 - 2 cm just below the orange mat. Methane
315 concentrations (Fig. 5F) under the orange mat ranged from less than 0.01 mM at the
316 surface to about 0.1 mM at the bottom of the core (Fig. 5F). AOM rates were highest in
317 the first few centimeters (13 nmol*cm^{-3}*d^{-1}). SR in these sediments also exceeded AOM
318 rates by 11-fold. Sulfide concentrations under the orange mat were below 0.01 mM. In
319 contrast, Fe(II) concentrations decreased from 0.7 mM just below the sediment surface to
320 zero below 16 cm sediment depth (Fig. 5G). Fe(II) was completely consumed in the

surface layer below the orange mat. Solid phase Fe and S contents (Table 3) were high throughout the core, but Fe was elevated in the orange mat and in the 5 - 7 cm zone. In view of the Fe and much lower S content, it is likely that both horizons contained substantial amounts of Fe oxides.

Organic carbon content (Table 3) in both cores were low (0.18 - 0.77%), which is typical for oligotrophic Eastern Mediterranean deep-sea sediments, indicating that the energy source for microbial reactions was not detritus-based.

CARD-FISH and FISH counts. Total cell numbers (Table 2) for both cores were around 10^9 cells*cm^{-3} in the upper 10 cm. In the white mat and its underlying sediment, total cell numbers decreased to 10^8 cells*cm^{-3} after 10 cm, whereas below the orange mat total cell numbers were more or less stable over the first 18 cm of sediment. Archaeal cells accounted for less than 3% of the total cells in both mats, but generally accounted for 12 - 38% of the total cells in the underlying sediments. In accordance with the biogeochemistry of the cores, anaerobic methanotrophic archaea (ANME) were detected in the top 6 cm of both cores (Table 2 and Fig. 6A,C). ANME-2 cells formed consortia with SRB belonging to the Desulfosarcina/Desulfococcus cluster (Fig. 6A). Free-living ANME-2 cells were not detected in the sediments. In contrast, ANME-3 were all single cells, and comprised 6 - 27% of the total cells in the 6 - 10 cm zone under the white mat and 7% in the 8 - 12 cm zone under the orange mat (Table 2 and Fig. 6B).

The mats as well as the top 2 cm of sediment from both cores were dominated by bacteria (52 - 67% of total cells in the sediments, Table 2). DSS658-targeted SRB made up less than 1% of the white mat community (Table 2 and Fig. 6C). They increased to 5 -

344 25% of the total cells in the top 6 cm of sediment underneath it, where the SR rate
345 maximum was detected, and dropped again to < 1% in deeper sediment. DSS658-targeted
346 SRB were more abundant in the orange mat and underlying sediment where they
347 comprised 8 - 19% of the total cells.
348 Arc94-targeted cells made up 8 - 24% of the white mat and top 4 cm of
349 underlying sediment (Table 2 and Fig. 3D). These cells comprised 4% of the total cells
350 within the orange mat and < 1% of the total cells in the underlying sediment. Type I
351 methanotrophs targeted by Mγ705 (Table 2, Fig 3H) comprised < 1% in the white mat
352 and in the sediment, but 2 - 8% in the orange mat and the 2 cm interval beneath it.
353
354 **16 rRNA gene analyses.** 16S rRNA gene libraries for bacteria were constructed for both
355 mats and the top 4 cm of sediment beneath them, whereas archaeal libraries were only
356 constructed for the sediments. Phylotypes identified in bacterial libraries from the mats as
357 well as the underlying sediment were very diverse, and corresponded to microorganisms
358 capable of many types of C, Fe, N, O and S transformations. The *Deltaproteobacteria*
359 represented the largest group of sequences from any of the libraries except from the
360 orange mat (Table 4 and Fig. 7). Most of these sequences were closely related to those of
361 the SRB clades *Desulfobacteraceae* and *Desulfobulbaceae*. Sequences belonging to
362 relatives of the *Desulfuromonadaceae* were recovered from the sediments underneath the
363 orange mat as well as from the white mat (Table 4 and Fig. 7). Members of this family
364 are capable of Fe(III) and S reduction (44, 69).
365 *Gammaproteobacteria* were the largest group of bacterial sequences (74 - 34%)
366 from the orange mat and a major group of sequences in the sediment underneath it (Table

4 and Fig. 8). Most of these sequences belonged to type I methanotrophs (46 - 12%), with the most closely related cultivated isolates (< 91% identity) being *Methylobacter marinus*, *Crenothrix polyspora*, *Clonothrix fusca* and others. Sequences most closely related (> 95% identity) to "Ca. A. sulfidicus" and *Sulfurimonas autotrophica* made up 32% of the sequences recovered from the white mat. Sequences closely related to those from *Sulfurospirillum arcachonense* (> 95% identity) were also recovered from both mats.

Sequences from ANME-2a, ANME-2c and ANME-3 made up 63 - 78% of archaeal sequences from the sediment below the white and orange mats (Table 4 and Fig. 9). ANME-3 sequences were only detected under the white mat and not under the orange, although ANME-3 cells were detected by FISH in both sediments. The ubiquitous seep- and subsurface sediment-associated groups of *Cren-* and *Euryarchaeota*, marine benthic groups B and D (MBGB and MBGD), respectively, made up significant portions (25 - 37%) of the sequences recovered from both cores.

Discussion

Primary productivity and organic matter fluxes to the seafloor have varied greatly in the history of the Eastern Mediterranean Sea, but today it is one of the most oligotrophic seas. Its bottom waters are fully oxygenated and organic matter flux to the seafloor is very low (9, 39, 62). Surface-exposed reduced sediments and accumulations of organisms, such as sulfide-oxidizing bacteria, tubeworms and bivalves (Figs 2 and 3) are clear indications of seepage of energy-rich compounds such as methane, higher

390 hydrocarbons, or sulfide. Living cold seep communities and biogeochemically active,
391 fluid-flow impacted sediments have been found along the Eastern Mediterranean Ridge
392 system (64) and the Nile Deep Sea Fan (5, 15, 65).
393 Generally at cold seeps, sites of high sulfide fluxes across the seafloor are marked
394 by mat-forming bacteria, which oxidize sulfide to sulfur or sulfate, using oxygen or
395 nitrate as the electron acceptor. These cells are often mobile and hence can bridge the gap
396 between sulfide and oxygen penetration in the sediments. The giant vacuolated sulfide
397 oxidizers store elemental sulfur internally, which gives the mats a characteristic white
398 color (31, 58, 63). Mats formed by giant vacuolated sulfide oxidizers typically appear
399 smooth (61), furry (attached vacuolated filamentous cells) (63) or crusty (i.e.
400 *Thiomargarita* spp. cold seep mats (31)). The mats described here have a different
401 appearance both macroscopically (cotton ball structure), as well as microscopically
402 (external sulfur storage).
403 To our knowledge, the orange mats have not been previously described from
404 marine cold seeps, but similar mats are known from a few hydrothermal vent settings (17,
405 36, 77) and ground water Fe(II) seeps (18). At these sites, they are thought to be created
406 by Fe(II)-oxidizing β- or γ-proteobacteria belonging to the genera *Gallionella*, *Leptothrix*
407 or *Marinobacter*, as well as the γ-proteobacterium PV-1. Both, the orange and white mats
408 investigated here appear to represent important communities at brine-impacted cold seeps
409 of the Eastern Mediterranean, and were commonly observed floating on the brine (white
410 mats, e.g. Fig 2F, H) or at the edge of brine lakes (orange mat, e.g. Fig. 2E).
411

412 **Composition of the white mats and orange mats.** The granules recovered from the
413 white mat were composed of elemental S filaments as shown by light microscopy, SEM
414 and EDX (Fig. 3). These filaments were most likely produced by chemoautotrophic
415 sulfide-oxidizing organisms related to "*Candidatus* Arcobacter sulfidicus" as indicated
416 by 16S rRNA gene analysis, and FISH, which showed that up to 25% of the cells within
417 the mat were made up by close relatives of this strain. "Ca. A. sulfidicus" secretes long S
418 filaments as a byproduct of sulfide oxidation (75), forming dense accumulations of
419 elemental S at hydrothermal vent settings (75), and in laboratory bioreactors (80). "Ca. A.
420 sulfidicus" has also been detected at cold seep settings (68). These environments are
421 typically sulfidic, high fluid-flow environments where sulfide and oxygen gradients
422 overlap due to advective processes.
423 Sequences closely related to *Desulfocapsa sulfoexigens*, which is capable of S
424 disproportionation into sulfide, sulfate and H^+ (20), represented another significant
425 portion of the sequences from the white mat. Their activities within this mat would likely
426 enhance S cycling as it would consume S, as well as provide additional sulfide.
427 The flakes that made up the orange mat were composed of Fe(III)-(hydr)oxide
428 encrusted sheaths (Fig. 3F,G) similar to those produced by the neutrophilic Fe(II)-
429 oxidizing *Betaproteobacterium Leptothrix ochracea* (87). Such sheaths have been shown
430 to be encrusted with Fe(III)-(hydr)oxides (35, 77) and were identified in several
431 hydrothermal vent settings (17, 36, 77). The metabolism of *Leptothrix ochracea* is
432 unclear as it has not been obtained in pure culture. Yet, it is generally regarded as a
433 heterotroph and is often found in organic-rich environments. It is unlikely that the low
434 organic carbon content of the Chefren sediments provide energy to heterotrophic mat-

435 forming iron-oxidizers (Table 3). Hence we speculate that the organisms responsible for
436 the mat formation are unknown chemoautotrophs, which gain energy from aerobic Fe(II)
437 oxidation utilizing the high flux of upward flowing, Fe(II) rich porewater.

438 Fe(II)-oxidizing bacteria are thought to form Fe-oxide encrusted sheaths in order
439 to locate the electron transfer process close to the cell as well as provide a means for the
440 cell to escape encrustation by Fe(III)-(hydr)oxides. The energetic yield of this process is
441 very low; therefore large amounts of Fe(II) need to be turned over in order to provide
442 enough energy for growth, leading to high amounts of Fe(III)-(hydr)oxide but very few
443 cells (17). Neutrophilic Fe(II) oxidation, although it occurs in a variety of environments,
444 such as hydrothermal vents (17), freshwater springs (28), and plant root nodules (19),
445 remains somewhat enigmatic, as under these conditions Fe(II) spontaneously oxidizes to
446 Fe(III). However, neutrophilic Fe(II)-oxidizing bacteria have been shown to increase Fe
447 oxidation rates by up to 4 times over abiotic rates (28, 59). The exact mechanism of this
448 process is currently unknown, but has been suggested to occur through the binding and
449 sequestration of Fe(II) by bacterial exopolymers (59).

450 It is possible that the Mγ705 targeted sheaths and related 16S rRNA gene
451 sequences obtained from the orange mat corresponded to organisms similar to *Crenothrix*
452 *polyspora* and *Clonothrix fusca* (90). They often occur bundled together as observed in
453 this study. It remains unclear as to whether these organisms can oxidize Fe(II) in addition
454 to methane, as they have only recently been cultivated. However, they are often found
455 environments where Fe(II) and methane co-occur, such as ground water springs.
456 Additionally, there are several literature reports of *C. polyspora* sheaths incrusted in
457 Fe(III)-(hydro)oxides (82, 91). No 16S rDNA sequences recovered from the orange mat

were similar to known Fe(II)-oxidizing species (e.g. sheath forming *Leptothrix* spp., stalk forming *Gallionella* spp., PV-1 and others).

In contrast, the orange mat contained many 16S rDNA sequences from bacteria that possibly constitute the reductive portion of the Fe cycle. Interestingly, sequences that grouped with *Sulfurospirillum deleyianum*, which is capable of Fe(III)-reduction via S cycling were detected within this mat (79). The presence of an active group of such microorganisms could couple and enhance S and Fe cycling, by oxidizing S compounds with Fe(III). Additionally, enrichments (Straub et. al, unpublished) using sediment from underneath the white mat with ferrihydrite as the sole electron acceptor, resulted in high numbers of *"Ca.* A. sulfidicus*"* sequences in the 16S rRNA gene libraries, suggesting that these organisms have a role in Fe(III) reduction.

Biogeochemical processes supporting white and orange microbial mat formation. Spatial heterogeneity in fluid flow on scales of meters to kilometers is known from several cold seep systems (47, 70). Here we observed large variations in fluid flow (Fig. 4) through microbial mats on scales of centimeters to meters associated with brine seepage. Brine seepage is a common feature of mud volcanoes from the Eastern Mediterranean Ridge (93, 94) and Western Province of the Nile Deep Sea Fan (23). These brines often co-migrate with hydrocarbons and sulfides (13, 88). Fluids from the brine pool at Chefren carried a high methane (2.4 mM) and sulfide (7.2 mM) concentration, a salinity of 150‰, and sulfate concentrations of around 50 mM (Caprais, pers. Comm.). Unfortunately we could not sample the brine flowing from black exposed sediments to the white mats (Fig. 2B), but it is likely that sulfide was present within the

481 brine, which precipitated Fe(II). The brine flow across the white mat likely impeded the
482 exchange with oxygenated water from the water column, providing a microaerophilic
483 environment for sulfide oxidation. Although, Cl^- and Na^+ profiles indicated upward fluid
484 flow, multidirectional (i.e. lateral and downward) advection cannot be ruled out.
485 Sulfide underneath the white mat was clearly provided by SR, rather than by
486 upward transport with brine (Fig. 5). The distribution of DSS658-targeted cells matched
487 the sulfide profile, as they displayed a maximum of 25% of the total cells between 0 - 2
488 cm (Table 2). Although our sampling resolution did not allow for the precise
489 determination of the limits of sulfide penetration, the rapid sulfide consumption at the
490 fluidic top of the core was likely due to the activity of *"Ca.* A. sulfidicus*"* and other
491 sulfide oxidizers. This environment is similar to high fluid flow environments (75, 80),
492 where sulfide and oxygen overlap due to advective processes and is likely to be a niche
493 for *"Ca.* A. sulfidicus*"* rather than for the giant vacuolated sulfide oxidizing bacteria.
494 Similar to the biogeochemistry of the white mat, SR rates under the orange mat were
495 significantly higher than AOM rates (Fig. 5). SRB cells reached 7 - 19% of total cells
496 under the orange mat. Maximum SR activity was located roughly at 4 - 10 cm, which
497 corresponded to increased amounts of solid phase Fe and S (Fig. 5). Sulfide produced in
498 this subsurface zone likely caused the precipitation of Fe and S complexes, similar to in
499 the sediment horizon directly under the white mat. No free sulfide was detected within
500 this core, therefore it is likely that the entire sulfide production went into the reduction of
501 Fe(III) and precipitation of Fe(II). The source of the very high free Fe(II) concentration
502 under the orange mat remains unknown; in-situ microbial Fe(III) reduction and upward
503 flow of Fe-rich subsurface fluids are plausible possibilities.

Bacterial community composition. As predicted from the markedly differing biogeochemistry, significant differences ($P < 1\%$) were detected in comparisons of bacterial 16S rRNA gene libraries obtained in this study, between both mats, as well as between the mats and their underlying sediments. The importance of SR was reflected by the high percentage of sequences (Table 4) belonging to members of the *Deltaproteobacteria* in both sediment libraries (31- 43%, Table 4). As expected these sequences grouped with those from genera of known sulfate reducers (Fig. 7) present at cold seeps, such as *Desulfobacter*, *Desulfosarcina*, *Desulfocapsa*, and *Desulfobulbus* (37) Some members of these genera are also capable of iron reduction (45), which occurred within the orange mat and in the underlying sediment. Sequences from members of the *Gammaproteobacteria* which are able to perform Fe(II) oxidation, sulfide oxidation, or methane oxidation were very prevalent in the libraries (10 - 73%). Most grouped with aerobic type I methanotrophs, such as *M. marinu*s, *C. polyspora* and *C. fusca* (Fig. 8), as well as with environmental sequences from methane rich sediments and symbionts in the gills of methanotrophic clams. Cultivated members of this group primarily oxidize methane with oxygen, but are also capable of oxidizing other C-1 compounds. As methane reached the top of both cores and was present in the water column, the sediment surface and especially the more oxidized orange mats represent potential niches for aerobic methanotrophy.

The high numbers of sequences of sulfur-oxidizing *Epsilonproteobacteria* (Fig. 8) in the white mat are consistent with the visual and biogeochemical data.

Archaeal community composition. Sixty to seventy percent of the archaeal sequences (Table 4) recovered from sediments underlying the orange and white mats belonged to the ANME-2 and ANME-3 clusters (Fig. 9). Their quantitative distribution differed between the sediments underlying the mats, and they overlapped only in one horizon (4-6 cm) under the white mat (Tab 3). In contrast, most other cold seeps typically showed a mix of ANME communities with a clear dominance of one community (38). The Chefren seep represents the second known cold seep habitat characterized by a relatively high abundance of ANME-3 cells (61). However, all of the ANME-3 cells that were detected were not associated with any bacterial partners. The remaining archaeal sequences comprised members of the marine benthic groups, (MBGB and MBGD) which are typical members of cold seep and subsurface communities (24, 38). However, no members of these two groups have been cultivated; therefore their roles in the sediments of Chefren and elsewhere remain unknown. Comparing the coverage of archaeal sequences from sediments underneath the white mat to those from underneath the orange mat a statistical difference ($P < 1\%$) was found, indicating a different community structure. The reciprocal test showed that the sediment community under the orange mat was not significantly different from that under the white mat ($P < 5\%$), possibly rather representing a subset of the white mat. It is possible that the archaeal community was more similar to each other than the bacterial community in the sediments because it largely comprised methanotrophs, which could be less affected by the differences in sulfide and iron biogeochemistry.

Comparison to other cold seep ecosystems. While fluid flow velocities and SR rates were similar to previously investigated cold seep systems, the associated AOM rates were comparatively low (60, 61, 65, 84, 86). The ratio between SR and methane oxidation rates of > 28:1 deviated strongly from the known stoichiometry of AOM of 1:1 to sulfate reduction (56). Hence, the sulfate reducing community apparently utilized compounds other than methane or organic detritus (Table 3). High rates of sulfate reduction exceeding anaerobic methane oxidation several fold are generally associated with seepage of higher hydrocarbons and petroleum (30, 41, 60, 65, 66). Besides methane, higher hydrocarbon compounds have been detected within the pore waters of Chefren and in the overlying water column and may fuel SR and Fe(III) reduction (Mastalerz, Unpublished data). Also, ANME-2 cells (Table 2) were only 8 - 25%, and ANME-3 cells 6 - 27% of total cells within this zone. These cell numbers, as well as the total cell numbers ($<10^9$ cells cm^{-3}) are lower than at other sites were AOM is the dominant biogeochemical process. Sites, such as Hydrate Ridge, the Black Sea and the Haakon Mosby mud volcano typically have ANME cell abundances of $>10^9$ cells cm^{-3} and were found to comprise >90% of total cell numbers (8, 37).

Conclusion. This study has elucidated some of the dominant microorganisms and processes involved in the formation of Fe(II)-oxidizing and sulfide-oxidizing mats at an active cold seep. Previously, these types of mats have only been described from hydrothermal vent settings, where sulfide and reduced iron was produced by seawater-rock interactions, and advected by venting. Our findings suggest that such mats could also be fueled by microbial sulfate reduction based on anaerobic hydrocarbon

degradation, maintained by relatively high fluid flow. Several questions still remain, such as the actual substrates fueling sulfate reduction, the rates of microbial vs. chemical Fe(II) and sulfide oxidation, the spatial relationship between the organisms that carry out these processes, and the ultimate fate of the end products (i.e. elemental S and Fe(III)-(hydr)oxide).

Acknowledgements

We thank the crews of the RV *L'Atalante* and the submersible *Nautile* as well as the NAUTINIL scientific party for their excellent work at sea. We thank Friederike Heinrich, Viola Beier and Tomas Wilkop for their initial processing of the samples, Claus Burkhardt for help with the electron microscope, Stefan Sievert for informing us about "*Candidatus* Arcobacter sulfidicus", Alban Ramette, Katrin Knittel for scientific suggestions and Casey Hubert for their helpful comments on this manuscript. The work of A.K. was supported by an Emmy-Noether fellowship from the German Research Foundation (DFG). The work of E.O. and A.B. in the ESF EUROCORES MEDIFLUX was financially supported by ESF, DFG and the Max Planck Society.

References

1. **Aharon, P., and B. Fu.** 2000. Microbial sulphate reduction rates and sulfur and oxygen isotope fractionations at oil and gas seeps in deepwater Gulf of Mexico. Geochim. Cosmochim. Acta **64:**233-246.

2. **Amann, R. I., L. Krumholz, and D. A. Stahl.** 1990. Fluorescent-oligonucleotide probing of whole cells for determinative, phylogenetic and environmental studies in microbiology. J. Bacteriol. **172:**762-770.

3. **Ashelford, K. E., N. A. Chuzhanova, J. C. Fry, A. J. Jones, and A. J. Weightman.** 2005. At least 1 in 20 16S rRNA sequence records currently held in public repositories is estimated to contain substantial anomalies. Appl. Environ. Microbiol. **71:**7724-7736.

4. **Ashelford, K. E., N. A. Chuzhanova, J. C. Fry, A. J. Jones, and A. J. Weightman.** 2006. New screening software shows that most recent large 16S rRNA gene clone libraries contain chimeras. Appl. Environ. Microbiol. **72:**5734-5741.

5. **Bayon, G., L. Loncke, S. Dupré, J.-C. Caprais, E. Ducassou, S. Duperron, J.-P. Foucher, Y. Fouquet, S. Gontharet, G. M. Henderson, J. Etoubleau, I. Klaucke, J. Mascle, S. Migeon, H. Ondréas, C. Pierre, C. Huguen, A. Stadnitskaia, J. Woodside, and M. Sibuet.** 2007. In situ investigation of the Centre Nile margin: Linking fluid seepage and continental-slope instabilities. Mar. Geol. **In review**.

6. **Boetius, A., T. Ferdelman, and K. Lochte.** 2000. Bacterial activity in sediments of the deep Arabian Sea in relation to vertical flux. Deep Sea Res. **47:**2835-2875.

7. **Boetius, A., and K. Lochte.** 1996. Effect of organic enrichments on hydrolytic potentials and growth of bacteria in deep-sea sediments. Mar. Ecol. Prog. Ser. **140:**239-250.

8. **Boetius, A., K. Ravenschlag, C. J. Schubert, D. Rickert, F. Widdel, A. Giesecke, R. Amann, B. B. Jørgensen, U. Witte, and O. Pfannkuche.** 2000. A marine microbial consortium apparently mediating anaerobic oxidation of methane. Nature **407:**623-626.

9. **Boetius, A., S. Scheibe, A. Tselepides, and H. Thiel.** 1996. Microbial biomass and activities in deep-sea sediments of the Eastern Mediterranean: trenches are benthic hotspots. Deep-Sea Res. **43:**1439-1460.

10. **Burdige, D. J., and K. H. Nealson.** 1986. Chemical and Microbiological Studies of Sulfide-Mediated Manganese Reduction. Geomicrobiol. J. **4:**361-387.

11. **Campbell, B. J., A. S. Engel, M. L. Porter, and K. Takai.** 2006. The versatile epsilon-proteobacteria: key players in sulphidic habitats. Nat. Rev. Microbiol. **4:**458-468.

12. **Daims, H., A. Brühl, R. Amann, and K. H. Schleifer.** 1999. The domain-specific probe EUB338 is insufficient for the detection of all Bacteria: Development and evaluation of a more comprehensive probe set. Syst. Appl. Microbiol. **22:**434-444.

13. **De Lange, G. J., and H. Brumsack, J.** 1998. The occurrence of gas hydrates in Eastern Mediteranean mud dome structures as indicated by porewater composition. Geol. Soc. Spec. **137:**167-175.

14. **Devereux, R., M. D. Kane, J. Winfrey, and D. A. Stahl.** 1992. Genus- and group specific hybridization probes for determinative and environmental studies of sulfate-reducing bacteria. Syst. Appl. Microbiol. **15:**601-609.

15. **Dupré, S., J. M. Woodside, J.-P. Foucher, G. de Lange, J. Mascle, A. Boetius, V. Mastalerz, A. Stadnitskaia, H. Ondreas, C. Huguen, F. Harmégnies, S. Gontharet, L. Loncke, E. Deville, H. Niemann, E. Omoregie, K. Olu-Le Roy, A. Fiala-Médioni, A. Dählmann, J.-C. Caprais, A. Prinzhofer, M. Sibuet, C. Pierre, J. Sinninghe Damsté, and N. S. Party.** 2007. Seafloor geological studies above active gas chimneys off Egypt (Central Nile Deep Sea Fan). Deep-Sea Res. **54:**1146-1172.

16. **Eller, G., S. Stubner, and P. Frenzel.** 2001. Group-specific 16S rRNA targeted probes for the detection of type I and type II methanotrophs by fluorescence in situ hybridisation. FEMS Microbiol. Lett. **198:**91-97.

17. **Emerson, D., and C. L. Moyer.** 2002. Neutrophilic Fe-Oxidizing Bacteria Are Abundant at the Loihi Seamount Hydrothermal Vents and Play a Major Role in Fe Oxide Deposition. Appl. Environ. Microbiol. **68:**3085-3093.

18. **Emerson, D., and N. P. Revsbech.** 1994. Investigation of an Iron-Oxidizing Microbial Mat Community Located near Aarhus, Denmark - Laboratory Studies. Appl. Environ. Microbiol. **60:**4032-4038.

19. **Emerson, D., J. V. Weiss, and J. P. Megonigal.** 1999. Iron-Oxidizing Bacteria Are Associated with Ferric Hydroxide Precipitates (Fe-Plaque) on the Roots of Wetland Plants. Appl. Environ. Microbiol. **65:**2758-2761.

20. **Finster, K., W. Liesack, and B. Thamdrup.** 1998. Elemental sulfur and thiosulfate disproportionation by *Desulfocapsa sulfoexigens* sp. nov., a new anaerobic bacterium isolated from marine surface sediment. Appl. Environ. Microbiol. **64:**119-125.

21. **Grasshoff, K., M. Ehrhardt, and K. Kremling.** 1983. p. 419, Methods of seawater analysis. Verlag Chemie, Weinheim.

22. **Hinrichs, K.-U., and A. Boetius.** 2002. The anaerobic oxidation of methane: new insights in microbial ecology and biogeochemistry, p. 457-477. *In* G. Wefer, D. Billett, D. Hebbeln, B. B. Joergensen, M. Schlüter, and T. Van Weering (ed.), Ocean Margin Systems. Springer-Verlag, Berlin.

23. **Huguen, C., J. P. Foucher, J. Mascle, H. Ondreas, M. Thouement, S. Gonthat, A. Stadnitskaia, C. Pierre, G. Bayon, L. Loncke, A. Boetius, I. Bouloubassi, G. d. Lange, Y. Fouquet, J. Woodside, and N. S. Party.** 2007. The Western Nile Margin Fluid seepages features: “in situ” observations of the Menes caldera (NAUTINIL Expedition, 2003). Mar. Geol. **In review**.

24. **Inagaki, F., M. M. M. Kuypers, U. Tsunogai, J. Ishibashi, K. Nakamura, T. Treude, S. Ohkubo, M. Nakaseama, K. Gena, H. Chiba, H. Hirayama, T. Nunoura, K. Takai, B. B. Jorgensen, K. Horikoshi, and A. Boetius.** 2006. Microbial community in a sediment-hosted CO2 lake of the southern Okinawa Trough hydrothermal system. Proc. Natl. Acad. Sci. USA **103:**14164-14169.

25. **Ishii, K., M. Mussmann, B. J. MacGregor, and R. Amann.** 2004. An improved fluorescence in situ hybridization protocol for the identification of bacteria and archaea in marine sediments. FEMS Microbiol. Ecol. **50:**203-213.

679 26. **Iversen, N., and T. H. Blackburn.** 1981. Seasonal rates of methane oxidation in
680 anoxic marine sediments. Appl. Environ. Microbiol. **41:**1295-1300.
681 27. **Iversen, N., and B. Jørgensen, B.** 1993. Diffusion Coefficients of Sulfate and
682 Methane in Marine Sediments Influence of Porosity. Geochim. Cosmochim. Acta
683 **57:**571-578.
684 28. **James, R. E., and F. G. Ferris.** 2004. Evidence for microbial-mediated iron
685 oxidation at a neutrophilic groundwater spring. Chem. Geol. **212:**301.
686 29. **Jørgensen, B., B.** 1978. A comparison of methods for the quantification of
687 bacterial sulfate reduction in coastal marine sediments. Measurement with
688 radiotracer techniques. Geomicrobiol. J. **1:**11-27.
689 30. **Joye, S. B., A. Boetius, B. N. Orcutt, J. P. Montoya, H. N. Schulz, M. J.**
690 **Erickson, and S. K. Logo.** 2004. The anaerobic oxidation of methane and sulfate
691 reduction in sediments from Gulf of Mexico cold seeps. Chem. Geol. **205:**219-
692 238.
693 31. **Kalanetra, K. M., S. B. Joye, N. R. Sunseri, and D. C. Nelson.** 2005. Novel
694 vacuolate sulfur bacteria from the Gulf of Mexico reproduce by reductive division
695 in three dimensions. Environ. Microbiol. **7:**1451-1460.
696 32. **Kallmeyer, J., T. G. Ferdelman, A. Weber, H. Fossing, and B. B. Jørgensen.**
697 2004. Evaluation of a cold chromium distillation procedure for recovering very
698 small amounts of radiolabeled sulfide related to sulfate reduction measurements.
699 Limnol. Oceanogr. Methods **2:**171-180.
700 33. **Kane, M. D., L. K. Poulsen, and D. A. Stahl.** 1993. Monitoring the enrichment
701 and isolation of sulfate-reducing bacteria by using oligonucleotide hybridization

probes designed from environmentally derived 16S rRNA sequences. Appl. Environ. Microbiol. **59:**682-686.

34. **Kasten, S., and B. Jørgensen, B.** 2000. Sulfate reduction in marine sediments, p. 263-281. *In* H. Schulze, D., and M. Zabel (ed.), Marine Geochemistry. Springer, Berlin.

35. **Kennedy, C. B., S. D. Scott, and F. G. Ferris.** 2003. Characterization of bacteriogenic iron oxide deposits from Axial Volcano, Juan de Fuca Ridge, northeast Pacific Ocean. Geomicrobiol. J. **20:**199-214.

36. **Kennedy, C. B., S. D. Scott, and F. G. Ferris.** 2003. Ultrastructure and potential sub-seafloor evidence of bacteriogenic iron oxides from axial volcano, Juan de Fuca Ridge, North-east Pacific Ocean. FEMS Microbiol. Ecol. **43:**247-254.

37. **Knittel, K., A. Boetius, A. Lemke, H. Eilers, K. Lochte, O. Pfannkuche, P. Linke, and R. Amann.** 2003. Activity, distribution, and diversity of sulfate reducers and other bacteria in sediments above gas hydrate (Cascadia margin, Oregon). Geomicrobiol. J. **20:**269-294.

38. **Knittel, K., T. Losekann, A. Boetius, R. Kort, and R. Amann.** 2005. Diversity and distribution of methanotrophic archaea at cold seeps. Appl. Environ. Microbiol. **71:**467-479.

39. **Krom, M. D., S. Brenner, L. Israilov, and B. Krumgalz.** 1991. Dissolved Nutrients, Preformed Nutrients and Calculated Elemental Ratios in the South-East Mediterranean-Sea. Oceanol. Acta **14:**189-194.

40. **Lane, D., B. Pace, G. Olsen, D. Stahl, M. Sogin, and N. Pace.** 1985. Rapid determination of 16S ribosomal RNA sequences for phylogenetic analyses. Proc. Natl. Acad. Sci. USA **82:**6955-6959.

41. **Lloyd, K. G., L. Lapham, and A. Teske.** 2006. Anaerobic methane-oxidizing community of ANME-1b archaea in hypersaline Gulf of Mexico sediments. Appl. Environ. Microbiol. **72:**7218-7230.

42. **Loncke, L., V. Gaullier, J. Mascle, B. Vendeville, and L. Camera.** 2006. The Nile deep-sea fan: An example of interacting sedimentation, salt tectonics, and inherited subsalt paleotopographic features. Mar. Pet. Geol. **23:**297-315.

43. **Lösekann, T., K. Knittel, T. Nadalig, B. Fuchs, H. Niemann, A. Boetius, and R. Amann.** 2007. Diversity and Abundance of Aerobic and Anaerobic Methane Oxidizers at the Haakon Mosby Mud Volcano, Barents Sea. Applied and Environmental Microbiology. Appl. Environ. Microbiol. **73:**3348-3362.

44. **Lovley, D. R., E. J. P. Phillips, D. J. Lonergan, and P. K. Widman.** 1995. Fe(III) and S^0 Reduction by *Pelobacter carbinolicus*. Appl. Environ. Microbiol. **61:**2132-2138.

45. **Lovley, D. R., E. E. Roden, E. J. P. Phillips, and J. C. Woodward.** 1993. Enzymatic iron and uranium reduction by sulfate-reducing bacteria. Mar. Geol. **113:**41.

46. **Ludwig, W., O. Strunk, R. Westram, L. Richter, H. Meier, Yadhukumar, A. Buchner, T. Lai, S. Steppi, G. Jobb, W. Forster, I. Brettske, S. Gerber, A. W. Ginhart, O. Gross, S. Grumann, S. Hermann, R. Jost, A. Konig, T. Liss, R. Lussmann, M. May, B. Nonhoff, B. Reichel, R. Strehlow, A. Stamatakis, N.**

Stuckmann, A. Vilbig, M. Lenke, T. Ludwig, A. Bode, and K.-H. Schleifer. 2004. ARB: a software environment for sequence data. Nucleic Acids Res. **32:**1363-1371.

47. **Luff, R., and K. Wallmann.** 2003. Fluid flow, methane fluxes, carbonate precipitation and biogeochemical turnover in gas hydrate-bearing sediments at Hydrate Ridge, Cascadia Margin: numerical modeling and mass balances. Geochim. Cosmochim. Acta **67:**3403-3421.

48. **Manz, W., R. Amann, W. Ludwig, M. Wagner, and K. H. Schleifer.** 1992. Phylogenetic oligodeoxynucleotide probes for the major subclasses of proteobacteria; problems and solutions. Syst. Appl. Microbiol. **15:**593-600.

49. **Mascle, J., L. Loncke, and L. Camera.** 2005. Geophysical evidences of fluid seepages and mud volcanoes on the Egyptian continental margin (Eastern Mediterranean). Boll. Soc. Geol. Ital.**:**127-134.

50. **Mascle, J., O. Sardou, L. Loncke, S. Migeon, L. Camera, and V. Gaullier.** 2006. Morphostructure of the Egyptian continental margin: Insights from swath bathymetry surveys. Mar. Geophys. Res. **27:**49-59.

51. **Massana, R., A. E. Murray, C. M. Preston, and E. F. DeLong.** 1997. Vertical distribution and phylogenetic characterization of marine planktonic Archaea in the Santa Barbara channel. Appl. Environ. Microbiol. **63:**50-56.

52. **Mau, S., H. Sahling, G. Rehder, E. Suess, P. Linke, and E. Soeding.** 2006. Estimates of methane output from mud extrusions at the erosive convergent margin off Costa Rica. Mar. Geol. **225:**129-144.

53. **Michaelis, W., R. Seifert, K. Nauhaus, T. Treude, V. Thiel, M. Blumenberg, K. Knittel, A. Gieseke, K. Peterknecht, T. Pape, A. Boetius, A. Aman, B. B. Jørgensen, F. Widdel, J. Peckmann, N. V. Pimenov, and M. Gulin.** 2002. Microbial reefs in the Black Sea fueled by anaerobic oxidation of methane. Science **297:**1013-1015.

54. **Mills, H. J., R. J. Martinez, S. Story, and P. A. Sobecky.** 2005. Characterization of microbial community structure in Gulf of Mexico gas hydrates: Comparative analysis of DNA- and RNA-derived clone libraries. Appl. Environ. Microbiol. **71:**3235-3247.

55. **Muyzer, G., A. Teske, C. O. Wirsen, and H. W. Jannasch.** 1995. Phylogenetic-Relationships of Thiomicrospira Species and Their Identification in Deep-Sea Hydrothermal Vent Samples by Denaturing Gradient Gel-Electrophoresis of 16S Rdna Fragments. Arch. Microbiol. **164:**165-172.

56. **Nauhaus, K., A. Boetius, M. Krüger, and F. Widdel.** 2002. In vitro demonstration of anaerobic oxidation of methane coupled to sulphate reduction in sediment from marine gas hydrate area. Environ. Microbiol. **4:**298-305.

57. **Neef, A.** 1997. Anwendung der in situ-Einzelzell-Identifizierung von Bakterien zur Populations-Analyse in komplexen mikrobiellen Biozönosen. Technische Universität München, München.

58. **Nelson, D. C., C. O. Wirsen, and H. W. Jannasch.** 1989. Characterization of Large, Autotrophic *Beggiatoa* Spp Abundant at Hydrothermal Vents of the Guaymas Basin. Appl. Environ. Microbiol. **55:**2909-2917.

59. **Neubauer, S. C., D. Emerson, and J. P. Megonigal.** 2002. Life at the Energetic Edge: Kinetics of Circumneutral Iron Oxidation by Lithotrophic Iron-Oxidizing Bacteria Isolated from the Wetland-Plant Rhizosphere. Appl. Environ. Microbiol. **68:**3988-3995.

60. **Niemann, H., J. Duarte, C. Hensen, E. Omoregie, V. H. Magalhaes, M. Elvert, L. M. Pinheiro, A. Kopf, and A. Boetius.** 2006. Microbial methane turnover at mud volcanoes of the Gulf of Cadiz. Geochim. Cosmochim. Acta **70:**5336.

61. **Niemann, H., T. Losekann, D. de Beer, M. Elvert, T. Nadalig, K. Knittel, R. Amann, E. J. Sauter, M. Schluter, M. Klages, J. P. Foucher, and A. Boetius.** 2006. Novel microbial communities of the Haakon Mosby mud volcano and their role as a methane sink. Nature **443:**854.

62. **Nijenhuis, I., A., H. Bosch, J., J. Sinninghe Damsté, S., H. Brumsack, J., and G. De Lange, J.** 1999. Organic matter and trace element rich sapropels and black shales: a geochemical comparison. Earth Planet. Sc. Lett. **169:**277-290.

63. **Nikolaus, R., J. W. Ammerman, and I. R. MacDonald.** 2003. Distinct pigmentation and trophic modes in *Beggiatoa* from hydrocarbon seeps in the Gulf of Mexico. Aquat. Microb. Ecol. **32:**85-93.

64. **Olu-Le Roy, K., M. Sibuet, A. Fiala-Medioni, S. Gofas, C. Salas, A. Mariotti, J. P. Foucher, and J. Woodside.** 2004. Cold seep communities in the deep eastern Mediterranean Sea: composition, symbiosis and spatial distribution on mud volcanoes. Deep-Sea Res. **51:**1915-1936.

65. **Omoregie, E. O., H. Niemann, V. Mastalerz, G. d. Lange, A. Stadnitskaia, J. Mascle, J.-P. Foucher, and A. Boetius.** Submitted. Anaerobic oxidation of methane and sulfate reduction at cold seeps in the Eastern Mediterranean Sea. Mar. Geol.

66. **Orcutt, B., A. Boetius, M. Elvert, V. Samarkin, and S. B. Joye.** 2005. Molecular biogeochemistry of sulfate reduction, methanogenesis and the anaerobic oxidation of methane at Gulf of Mexico cold seeps. Geochim. Cosmochim. Acta **69:**4267-4281.

67. **Reitz, A., J. Thomson, G. J. de Lange, and C. Hensen.** 2006. Source and development of large manganese enrichments above eastern Mediterranean sapropel S1. Paleoceanography **21:**PA3007.

68. **Robinson, C. A., J. M. Bernhard, L. A. Levin, G. F. Mendoza, and J. K. Blanks.** 2004. Surficial Hydrocarbon Seep Infauna from the Blake Ridge (Atlantic Ocean, 2150 m) and the Gulf of Mexico (690–2240 m). Mar. Ecol. Prog. Ser. **25:**313-336.

69. **Roden, E. E., and D. R. Lovley.** 1993. Dissimilatory Fe(III) Reduction by the Marine Microorganism *Desulfuromonas-Acetoxidans*. Appl. Environ. Microbiol. **59:**734-742.

70. **Sahling, H., D. Rickert, R. W. Lee, P. Linke, and E. Suess.** 2002. Macrofaunal community structure and sulfide flux at gas hydrate deposits from the Cascadia convergent margin, NE Pacific. Mar. Ecol. Prog. Ser. **231:**121-138.

71. **Sassen, R., S. L. Losh, I. L. Cathles, H. H. Roberts, J. K. Whelan, A. V. Milkov, S. T. Sweet, and D. A. DeFreitas.** 2001. Massive vein-filling gas

hydrate: relation to ongoing gas migration from the deep subsurface in the Gulf of Mexico. Mar. Pet. Geol. **18:**551.

72. **Sassen, R., H. H. Roberts, P. Aharon, J. Larkin, E. W. Chinn, and R. Carney.** 1993. Chemosynthetic bacterial mats at cold hydrocarbon seeps, Gulf of Mexico continental slope. Org. Geochem. **20:**77.

73. **Schloss, P. D., B. R. Larget, and J. Handelsman.** 2004. Integration of microbial ecology and statistics: a test to compare gene libraries. Appl. Environ. Microbiol. **70:**5485-5492.

74. **Sibuet, M., and K. Olu.** 1998. Biogeography, biodiversity and fluid dependence of deep-sea cold-seep communities at active and passive margins. Deep Sea Res. **45:**517-567.

75. **Sievert, S. M., E. B. A. Wieringa, C. O. Wirsen, and C. D. Taylor.** 2006. Growth and mechanism of filamentous-sulfur formation by *Candidatus* Arcobacter sulfidicus in opposing oxygen-sulfide gradients. Environ. Microbiol. **9:**271-276.

76. **Snaidr, J., R. Amann, I. Huber, W. Ludwig, and K. H. Schleifer.** 1997. Phylogenetic analysis and in situ identification of bacteria in activated sludge. Appl. Environ. Microbiol. **63:**2884-2896.

77. **Staudigel, H., S. R. Hart, A. Pile, B. E. Bailey, E. T. Baker, S. Brooke, D. P. Connelly, L. Haucke, C. R. German, I. Hudson, D. Jones, A. A. P. Koppers, J. Konter, R. Lee, T. W. Pietsch, B. M. Tebo, A. S. Templeton, R. Zierenberg, and C. M. Young.** 2006. Vailulu'u Seamount, Samoa: Life and death on an active submarine volcano. Proc. Natl. Acad. Sci. USA **103:**6448-6453.

78. **Stoecker, K., B. Bendinger, B. Schöning, P. H. Nielsen, J. L. Nielsen, C. Baranyi, E. R. Toenshoff, H. Daims, and M. Wagner.** 2006. Cohn's *Crenothrix* is a filamentous methane oxidizer with an unusual methane monooxygenase. Proc. Natl. Acad. Sci. USA **103:**2363-2367.

79. **Straub, K. L., and B. Schink.** 2004. Ferrihydrite-dependent growth of *Sulfurospirillum deleyianum* through electron transfer via sulfur cycling. Appl. Environ. Microbiol. **70:**5744-5749.

80. **Taylor, C. D., and C. O. Wirsen.** 1997. Microbiology and ecology of filamentous sulfur formation. Science **277:**1483-1485.

81. **Taylor, C. D., C. O. Wirsen, and F. Gaill.** 1999. Rapid microbial production of filamentous sulfur mats at hydrothermal vents. Appl. Environ. Microbiol. **65:**2253-2255.

82. **Taylor, S. W., C. R. Lange, and E. A. Lesold.** 1997. Biofouling of contaminated ground-water recovery wells: Characterization of microorganisms. Ground Water **35:**973-980.

83. **Thamdrup, B., H. Fossing, and B. Jørgensen, B.** 1994. Manganese, iron, and sulfur cycling in a coastal marine sediment, Aarhus Bay, Denmark. Geochim. Cosmochim. Acta **58:**5115-5129.

84. **Treude, T., A. Boetius, K. Knittel, K. Wallmann, and B. B. Jørgensen.** 2003. Anaerobic oxidation of methane above gas hydrates at Hydrate Ridge, NE Pacific Ocean. Mar. Ecol. Prog. Ser. **264:**1-14.

85. **Treude, T., K. Knittel, M. Blumenberg, R. Seifert, and A. Boetius.** 2005. Subsurface microbial methanotrophic mats in the Black Sea. Appl. Environ. Microbiol. **71:**6375-6378.

86. **Treude, T., J. Niggemann, J. Kallmeyer, P. Wintersteller, C. J. Schubert, A. Boetius, and B. B. Jorgensen.** 2005. Anaerobic oxidation of methane and sulfate reduction along the Chilean continental margin. Geochim. Cosmochim. Acta **69:**2767-2779.

87. **van Veen, W., L., E. G. Mulder, and M. Deinema.** 1978. The *Spaerotilus-Leptothrix* Group of Bacteria. Microbiol. Rev. **42:**329-356.

88. **vanSantvoort, P. J. M., and G. J. deLange.** 1996. Messinian salt fluxes into the present-day eastern Mediterranean: Implications for budget calculations and stagnation. Mar. Geol. **132:**241-251.

89. **vanSantvoort, P. J. M., G. J. deLange, J. Thomson, H. Cussen, T. R. S. Wilson, M. D. Krom, and K. Strohle.** 1996. Active post-depositional oxidation of the most recent sapropel (S1) in sediments of the eastern Mediterranean Sea. Geochim. Cosmochim. Acta **60:**4007-4024.

90. **Vigliotta, G., E. Nutricati, E. Carata, S. M. Tredici, M. De Stefano, P. Pontieri, D. R. Massardo, M. V. Prati, L. De Bellis, and P. Alifano.** 2007. *Clonothrix fusca Roze* 1896, a Filamentous, Sheathed, Methanotrophic γ-Proteobacterium. Appl. Environ. Microbiol. **73:**3556-3565.

91. **Volker, H., R. Schweisfurth, and P. Hirsch.** 1977. Morphology and Ultrastructure of *Crenothrix Polyspora* Cohn. J. Bacteriol. **131:**306-313.

92. **Wallner, G., I. Steinmetz, D. Bitter-Suermann, and R. Amann.** 1996. Flow cytometric analysis of activated sludge with rRNA-targeted probes. Appl. Environ. Microbiol. **19:**569-576.

93. **Woodside, J., M.** 2000. Linking Mediterranean brine pools and mud volcanism. EOS Transactions of the American Geophysical Union **81**.

94. **Woodside, J. M., and A. V. Volgin.** 1996. Brine pools associated with Mediterranean Ridge mud diapirs: an interpretation of echo-free patches in deep tow sidescan sonar data. Mar. Geol. **132:**55-61.

95. **Zitter, T. A. C., C. Huguen, and J. M. Woodside.** 2005. Geology of mud volcanoes in the eastern Mediterranean from combined sidescan sonar and submersible surveys. Deep-Sea Res. **52:**457-475.

Probe	Target Group	Sequence (5' to 3')	Type	% Formamide	°C Hybrid/Wash	Reference
ARCH915	Most Archaea	GTGCTCCCCCGCCAATTCCT	CARD	35	46/48	(2)
ANME-1-350	ANME-1	AGTTTTCGCGCCTGATGC	CARD	40	46/48	(6)
ANME-2-538	ANME-2	GGCTACCACTCGGGCCGC	FISH	50	46/48	(85)
ANME-3-1249	ANME-3	TCGGAGTAGGGACCCATT	CARD	20	46/48	(43)
EUB I	Most Bacteria	GCTGCCTCCCGTAGGAGT	CARD	35	46/48	(2)
EUB II	Planctomycetales	GCAGCCACCCGTAGGTGT	CARD	35	46/48	(12)
EUB III	Verrucomicrobiales	GCTGCCACCCGTAGGTGT	CARD	35	46/48	(12)
Non338	negative hybridization probe	ACTCCTACGGGAGGCAGC	CARD/FISH	variable	46/48	(92)
Alf968	Alphaproteobacteria	GGTAAGGTTCTGCGCGTT	FISH	35	46/48	(57)
Gam42	Gammaproteobacteria	GCCTTCCCACATCGTTT	FISH	35	46/48	(48)
Beta42a	Betaproteobacteria	GCCTTCCCACTTCGTTT	FISH	35	46/48	(48)
DSS658	*Desulfosarcina/Desulfococcus*	TCCACTTCCCTCTCCCAT	CARD	50	46/48	(48)
660	*Desulfobulbus*	GAATTCCACTTTCCCCTCTG	CARD	60	46/48	(14)
Mγ705	Type I methanotrophs	CTGGTGTTCCTTCAGATC	FISH	20	46/48	(16)
Arc94	*Arcobacter*	TGCGCCACTTAGCTGACA	CARD	20	46/48	(76)

914

915

916 **Table 1.** Oligonucleotide probes and hybridization conditions used in this study. EUB-I, II, III were mixed into a single solution.

			ARC915			ANME-2			ANME-3		
	Depth	Total cells $1x10^9$	Free cells $1x10^9$	Cells in Agg $1x10^9$	Percent Total cells	Free cells $1x10^9$	Cells in Agg $1x10^9$	Percent Dapi	Free cells $1x10^9$	Cells in Agg $1x10^9$	Percent Total cells
NL18PC5	mat	1.00	0.03	<	3	<	<	<	<	<	nd
	0-2cm	0.90	0.14	<	16	<	<	<	<	<	nd
	2-4cm	2.10	0.18	0.59	37	<	0.38	18	<	<	nd
	4-6cm	1.97	0.18	0.52	36	<	0.50	25	0.14	<	7
	6-8cm	0.61	0.19	<	31	<	nd	<	0.17	<	27
	8-10cm	1.10	0.20	<	18	<	nd	<	0.07	<	6
	10-12cm	0.42	0.07	<	18	<	nd	<	<	<	nd
	12-14cm	0.20	0.02	<	12	<	nd	<	<	<	nd
	14-16cm	0.20	0.03	<	14	<	nd	<	<	<	nd
	16-18cm	0.24	nd	nd	nd	<	nd	nd	<	<	nd
NL18PC8	mat	0.80	0.02	<	3	<	nd	<	<	<	nd
	0-2cm	1.28	0.03	0.07	8	<	0.10	8	<	<	nd
	2-4cm	4.75	0.95	0.84	38	<	0.96	20	<	<	nd
	4-6cm	0.76	0.19	<	25	<	nd	<	<	<	nd
	6-8cm	1.15	0.25	<	22	<	nd	<	<	<	nd
	8-10cm	1.09	0.16	<	14	<	nd	<	0.08	<	7
	10-12cm	0.91	0.24	<	26	<	nd	<	0.06	<	7
	12-14cm	1.60	0.24	<	15	<	nd	<	<	<	nd
	14-16cm	0.97	0.15	<	16	<	nd	<	<	<	nd
	16-18cm	0.62	0.09	<	14	<	nd	<	<	<	nd

			EUBI-III			DSS658			ARC94			Mγ705		
	Depth	Total cells $1x10^9$	Free cells $1x10^9$	Cells in Agg $1x10^9$	Percent Total cells	Free cells $1x10^9$	Cells in Agg $1x10^9$	Percent Total cells	Free cells $1x10^9$	Cells in Agg $1x10^9$	Percent Total cells	Free cells $1x10^9$	Cells in Agg $1x10^9$	Percent Total cells
NL18PC5	mat	1.00	0.67	<	67	<	<	nd	0.24	<	24	0.003	<	0.31
	0-2cm	0.90	0.47	<	52	0.21	<	23	0.20	<	22	<	<	nd
	2-4cm	2.10	0.49	0.59	51	0.17	0.33	23	0.10	<	5	<	<	nd
	4-6cm	1.97	0.29	0.52	42	0.07	0.23	24	0.01	<	1	<	<	nd
	6-8cm	0.61	0.15	<	25	0.03	<	5	<	<	nd	<	<	nd
	8-10cm	1.10	0.41	<	37	<	<	nd	<	<	nd	<	<	nd
	10-12cm	0.42	0.13	<	30	<	<	nd	<	<	nd	<	<	nd
	12-14cm	0.20	0.12	<	60	<	<	nd	<	<	nd	<	<	nd
	14-16cm	0.20	0.02	<	11	<	<	nd	<	<	nd	<	<	nd
	16-18cm	0.24	nd	<	nd	<	<	nd	<	<	nd	<	<	nd
NL18PC8	mat	0.80	0.54	<	67	0.08	<	10	0.03	<	4	0.06	<	8
	0-2cm	1.28	0.78	0.07	66	0.17	0.07	19	0.04	<	nd	0.03	<	2
	2-4cm	4.75	1.09	0.84	41	0.32	1.92	7	0.03	<	nd	<	<	nd
	4-6cm	0.76	0.27	<	36	0.06	<	8	<	<	nd	<	<	nd
	6-8cm	1.15	0.30	<	26	0.14	<	12	<	<	nd	<	<	nd
	8-10cm	1.09	0.38	<	35	0.03	<	3	<	<	nd	<	<	nd
	10-12cm	0.91	0.16	<	17	0.09	<	10	<	<	nd	<	<	nd
	12-14cm	1.60	0.65	<	41	0.16	<	10	<	<	nd	<	<	nd
	14-16cm	0.97	0.39	<	40	0.11	<	12	<	<	nd	<	<	nd
	16-18cm	0.62	0.15	<	24	nd	<	nd	<	<	nd	<	<	nd

Table. 2 Fluorescence in Situ Hybridization counts for the white and orange mats as well the underlying sediments. "Total cells" indicate cell numbers obtained with AODC. Counts for probe ANME-1 and 660 were both below 1% of the total cells in all samples. "<" indicates numbers were less than 0.1% of the total cells. "nd" indicates not determined.

White Mat Depth (cm)	Corg (% w/w)	Cl (mM)	Na (mM)	Fe (% w/w)	S (% w/w)
Bottom water	-	863	704	-	
0-2 cm	-	1487	1240	13.6	11.35
2-4 cm	0.70	1545	1209	17.14	15.54
4-6 cm	0.44	1657	1282	5.10	2.10
6-8 cm	0.77	1627	1317	13.87	12.47
8-10 cm	0.24	1602	1317	3.50	<
10-12 cm	0.23	1571	1293	5.00	<
12-14 cm	0.22	1567	1244	4.85	<
14-16 cm	0.21	1573	1332	5.23	<
16-18 cm	0.18	-	1380	2.51	<
18-20 cm	0.21	-	1301	2.17	<

Orange Mat Depth (cm)	Corg (% w/w)	Cl (mM)	Na (mM)	Fe (% w/w)	S (% w/w)
Bottom water	-	657	565	-	
mat	-	-	-	11.62	3.51
0.75 cm	0.60	824	737	5.08	2.37
1-3 cm	0.53	1020	913	4.34	1.80
3-5 cm	0.44	1151	1011	4.32	1.45
5-7 cm	0.61	1239	1099	7.77	1.19
7-9 cm	0.56	1031	871	4.88	2.03
9-11 cm	0.57	1370	1187	5.06	2.46
11-13 cm	0.58	1375	1235	5.19	2.50
13 - 15 cm	0.56	1388	1242	4.84	2.04
15 - 17 cm	-	-	1153	-	-

Table 3. Pore water and solid phase geochemical profiles of the white and orange mats as well as the underlying sediments.

Phylogenetic group	White mat	White mat (Sediment)	Organge mat	Orange mat (sediment)
Total number of bacterial clones	**91**	**83**	**120**	**88**
% *Alphaproteobacteria*	**1**	**0**	**3**	**1**
% *Gammaproteobacteria*	**2**	**8**	**74**	**34**
Type I methanotrophs	0	2	42	7
% *Deltaproteobacteria*	**32**	**42**	**7**	**31**
Desulfobacteraceae (*Desulfosarcina variabilis*)	2(0)	30(23)	1(0)	16(10)
Desulfobulbaceae (*Desulfocapsa sulfexigens*)	20(20)	8(6)	6(0)	10(1)
Desulfuromonadaceae	9	0	0	1
% *Epsilonproteobacteria*	**36**	**0**	**12**	**7**
"Candidatus Arcobacter Sulfidicus"	2	0	1	0
Sulfurospirillum arcachonense	2	0	0	0
Sulfurimonas autotrophica	30	0	0	0
% Other bacteria	**29**	**42**	**5**	**22**
% Unidentified bacteria	**0**	**7**	**0**	**6**
Total number of archaeal clones		**71**		**66**
% *Euryarchaeota*		**96**		**98**
Possible ANME		0		3
ANME-2A		18		52
ANME-2C		1		3
ANME-3		55		0
MBG-D		15		36
% *Crenarchaeota*		**4**		**2**
MBG-B		4		2
MBG-1		0		0

Table 4. Breakdown of 16S rRNA gene sequence groupings, in percentages obtained from the white and orange mats as well as the top 4 cm of sediment beneath them.

930 **Figure Legends**

931

932 Figure 1. (A) Bathymetric map of the Nile Deep Sea Fan (NDSF), kindly provided by
933 Jean Mascle, Geosciences Azur (49) The circle indicates the position of the Menes
934 Caldera. (B) Bathymetric map of the Menes Caldera with its three mud volcano systems.
935 (C) Bathymetric map of the Chefren mud volcano. "X" indicates the location close to
936 Chefren characterized by orange and white mats, the circle indicates the location of brine
937 samples obtained during *Nautile* Dive18. Both maps in B and C were obtained during
938 METEOR expedition BIONIL M70/2 in 2006 using the EM120 multibeam.

939

940 Figure 2. The microbial mat system of the brine-impacted seep at the rim of the Chefren
941 mud volcano. (A) Photograph taken by the submersible *Nautile*, at the recovery site of the
942 orange and white mats. On the right side, the sediments are populated by sessile worms
943 (arrows) forming tubes from sediment particles. Scale bar is 3 m. (B) Close up of the mat
944 system. Brine flowed downward (arrows) from the steep rim of the Chefren mud volcano
945 across the white mats. Scale bar is 1 m. (C) Photographs of a core from the white mat.
946 Left: The black to grey sediment layers below the white mat. Middle: Top of the core:
947 The white mat was composed of cotton ball-like precipitates overlying black fluidic
948 sediments. Scale bar is 3 cm (corresponds to middle image). Insert: small motile
949 polychaetes associated with white mat and the black sediment layer. The red color of the
950 polychaetes indicates elevated hemoglobin levels, a typical adaptation to reduced
951 sediments. Scale bar is 0.5 cm. (D) Photographs of a core from the orange mat. Left: the
952 greyish sediment layers below the orange mat. Middle: top of the core. Arrows indicates

953 a sessile worm (top), the orange fluffy material and flakes (bottom) overlaying grayish
954 sediments. Scale bar is 3 cm (corresponds to middle image). (E) Orange precipitates on
955 sediments at the border of the brine lake. Scale bar is 20 cm. (F) Dense white mats
956 floating on top of the large brine lake filling the center of the Chefren mud volcano. Scale
957 bar is 3 m.
958
959 Figure 3. (A) Dissecting microscope image of a S aggregate from the white mat. Scale
960 bar indicates 1 mm. (B) Phase contrast image of S filaments from the white mat. Scale
961 bar is 10 μm (C) High resolution SEM image of filaments and associated cells from the
962 white mat. (D) FISH image showing ARC94 targeted cells (green). (E) Image of Fe-
963 oxide flakes from the orange mat. (F) Light microscope image from an orange flake. (G)
964 High resolution SEM image of damaged sheaths from a flake. Arrows indicate two
965 distinct types of sheathed bacteria (bacteria are not visible, just their sheaths). (H) FISH
966 image showing Mγ705 targeted sheaths. Arrows indicate two distinct types of sheathed
967 bacteria similar to *Clonothrix fusca* (1) and *Crenothrix polyspora* (2). Scale bars for B-D
968 and F-H indicate 10 μm. Cores NL18PC3(5) and NL18PC1(8) were used for microscopy.
969
970 Figure 4. Cl^- profiles from fluid flow models. (A) Measured Cl^- profile from underneath
971 the white mats (circles), modeled Cl^- profile at a constant flow of 15 $m*a^{-1}$ (straight line)
972 and modeled Cl^- profile after 10 h zero fluid flow velocity (dashed line). (B) Measured
973 Cl^-profile from underneath the orange mats (circles), modeled Cl^- profile at a constant
974 flow of 0.6 $m*a^{-1}$ (straight line) and modeled Cl^- profile after 10 h at zero fluid flow
975 velocity (dashed line).

Figure 5. (A) Replicate sulfate reduction rate measurements (circles) and sulfate measurements (triangles) underneath the white mats. (B) Replicate rates of methane oxidation (circles) and methane measurements (triangles) from underneath the white mats. (C) Fe(II) (white circles) and HS^- (black circles) concentrations from underneath the white mats. (D) Sedimentological description of the sediment underneath the white mats. (E) Replicate sulfate reduction rate measurements (circles) and sulfate measurements (triangles) from underneath the orange mats. (F) Replicate methane oxidation rate measurements (circles) and methane measurements (triangles) from underneath the orange mats. (G) Fe(II) (white circles) and HS^- (black circles) concentrations from underneath the orange mats. (H) Sedimentological description of the sediment underneath the orange mats.

Figure 6. (A) Double hybridization using FISH probes ANME2-538 (red) and DSS658 (green). (B) ANME3-1249 targeted cells. (C) DSS658 targeted cells. (D) Mγ705 targeted single cells. All bars indicate 10 µm. Cores NL18PC3(5) and NL18PC1(8) were used for microscopy.

Figure 7. Maximum-parsimony tree of 16S rRNA gene sequences from *Deltaproteobacteria* obtained in this study, as well as from the GenBank database. Names in brackets are from well-known cold seeps and hydrothermal vents. The bootstrap values on the nodes are percentages out of 500 replicates. Sequences from this study are indicated in bold, and the numbers in brackets indicate the number of sequences

within 98% identity to the relevant sequence from the white mat, underlying sediment, the orange mat and its underlying sediment. Only selected sequences are displayed in the tree. Sequences that are targeted by the DSS658 and the 660 probes are indicated.

Figure 8. Maximum-parsimony tree of 16S rRNA gene sequences from *Gamma-, Beta-,* and *Epsilonproteobacteria*, and unidentified sequences obtained in this study, as well as from the GenBank database. The bootstrap values on the nodes are percentages out of 500 replicates. Names in brackets are from well-known cold seeps and hydrothermal vents. Sequences from this study are indicated in bold, and the 4 numbers in brackets indicate the number of sequences within 98% identity to the relevant sequence from the white mat, underlying sediment, the orange mat and its underlying sediment. Only selected sequences are displayed in the tree. Sequences that are targeted Arc94 and Mγ705 are indicated.

Figure 9. Maximum-parsimony tree of 16S rRNA gene sequences from *Achaea* obtained in this study, as well as from the GenBank database. Names in brackets are from well-known cold seeps and hydrothermal vents. The bootstrap values on the nodes are percentages out of 500 replicates. Sequences from this study are indicated in bold, and the numbers in brackets indicate the number of sequences within 98% identity to the relevant sequence from the white mat, underlying sediment, the orange mat and its underlying sediment. Only selected sequences are displayed in the tree. The sequence with accession number DQ369741 was excluded from bootstrap analysis and added to the

1021 tree using the parsimony tool in ARB. Sequences that are targeted by ANME-1-350,

1022 ANME-2-538 and ANME-3-1249 are indicated.

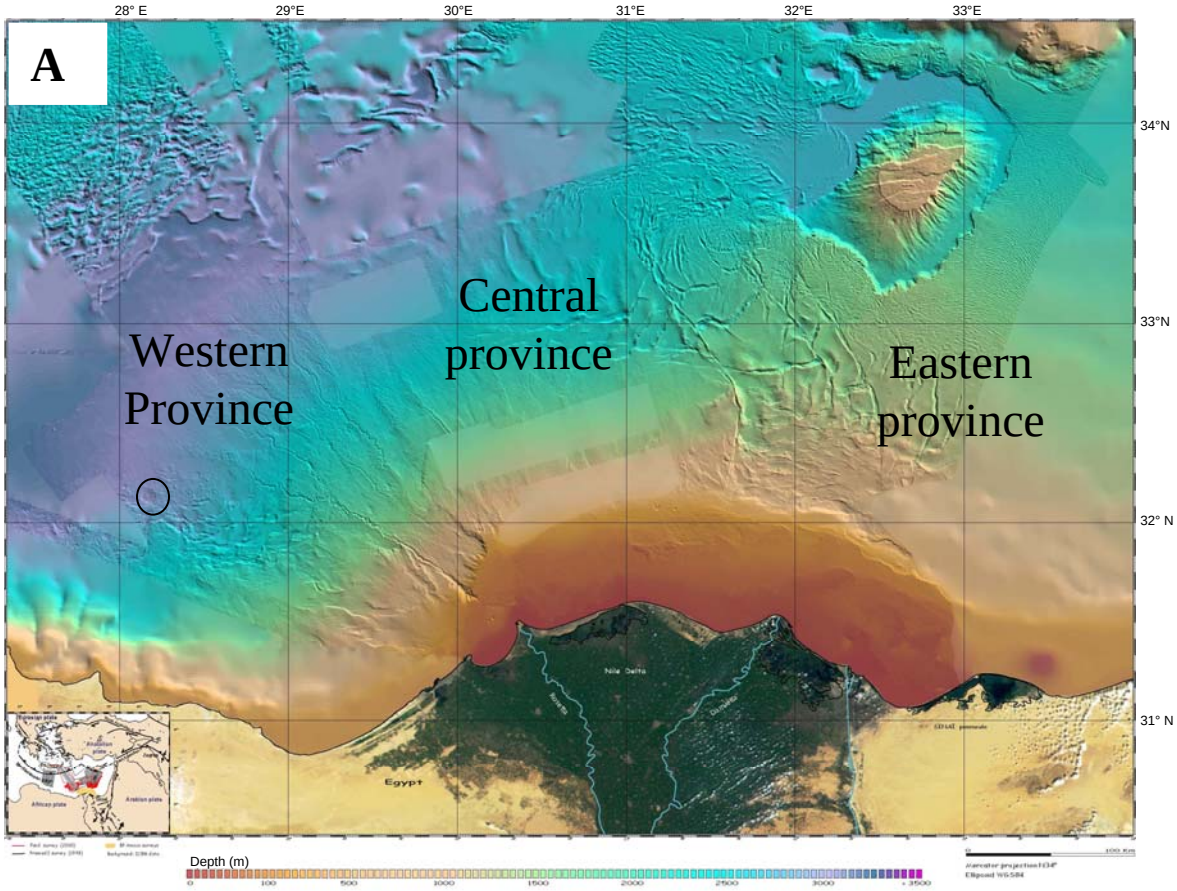
A
28° E
29°E
30°E
31°E
32°E
33°E
34°N
33°N
32° N
31° N
Western
Province
Central
province
Eastern
province
Egypt
Depth (m)

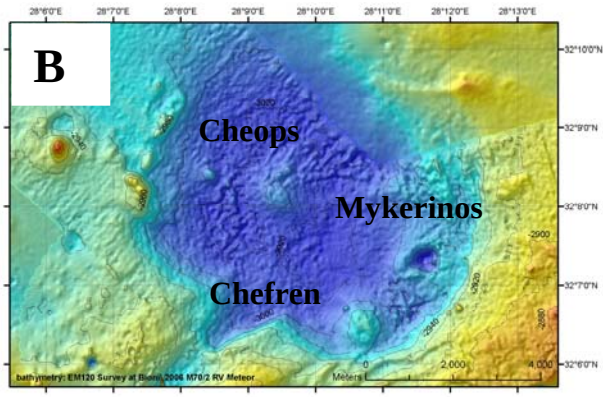
B
Cheops
Mykerinos
Chefren
bathymetry: EM120 Survey at Bionil 2006 M70/2 RV Meteor
Meters

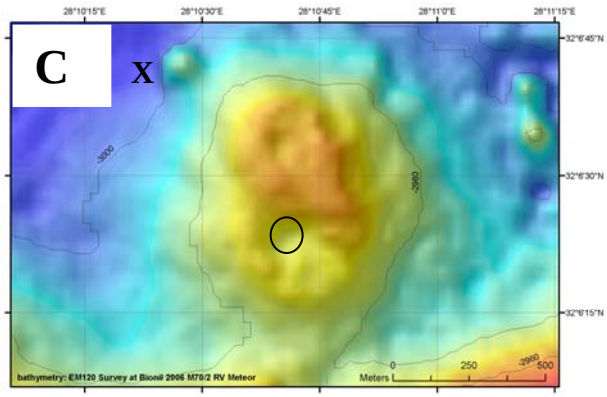
C
x
bathymetry: EM120 Survey at Bionil 2006 M70/2 RV Meteor
Meters

Figure 1

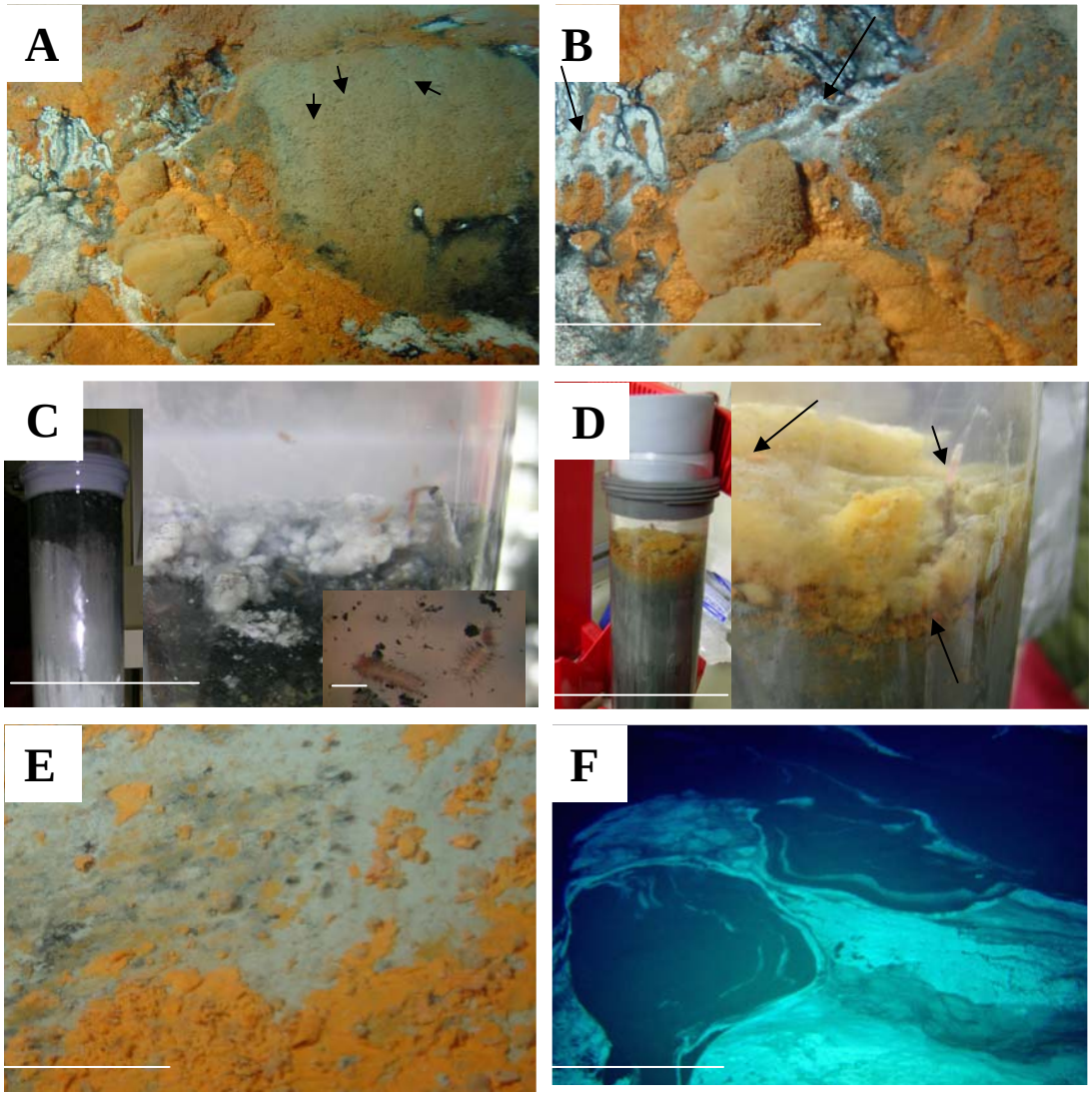

Figure 2

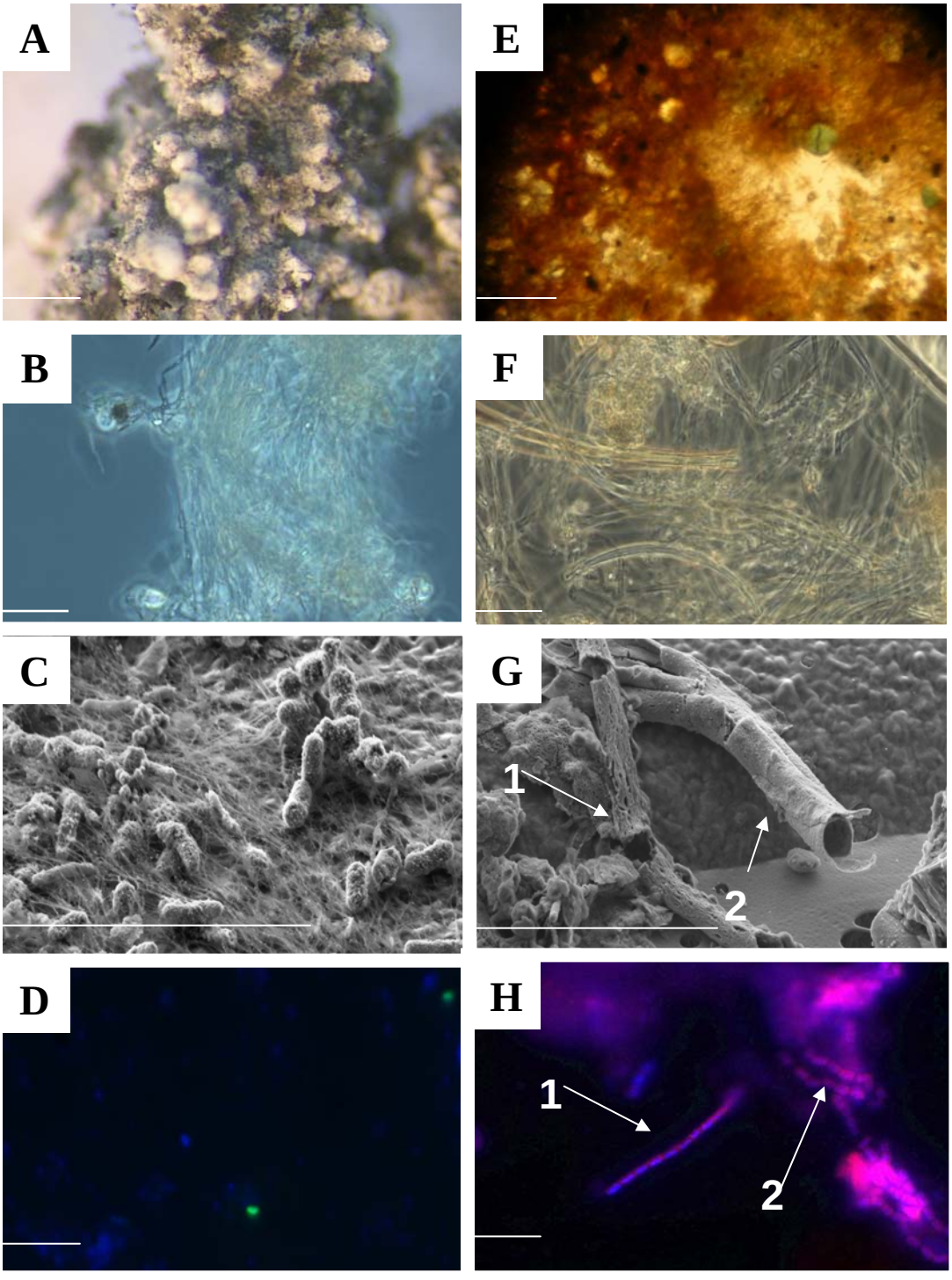

Figure 3

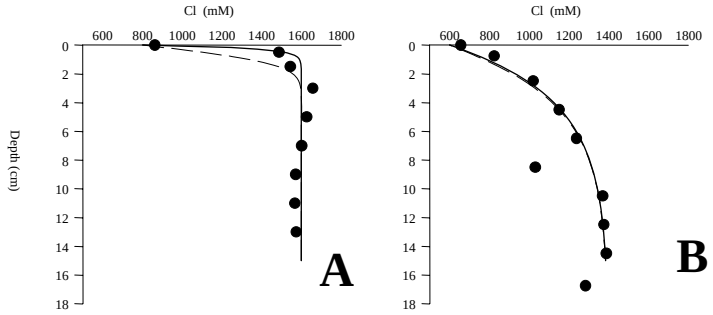
Cl (mM)
600 800 1000 1200 1400 1600 1800
0 2 4 6 8 10 12 14 16 18
Depth (cm)
A
Cl (mM)
600 800 1000 1200 1400 1600 1800
0 2 4 6 8 10 12 14 16 18
B

Figure 4

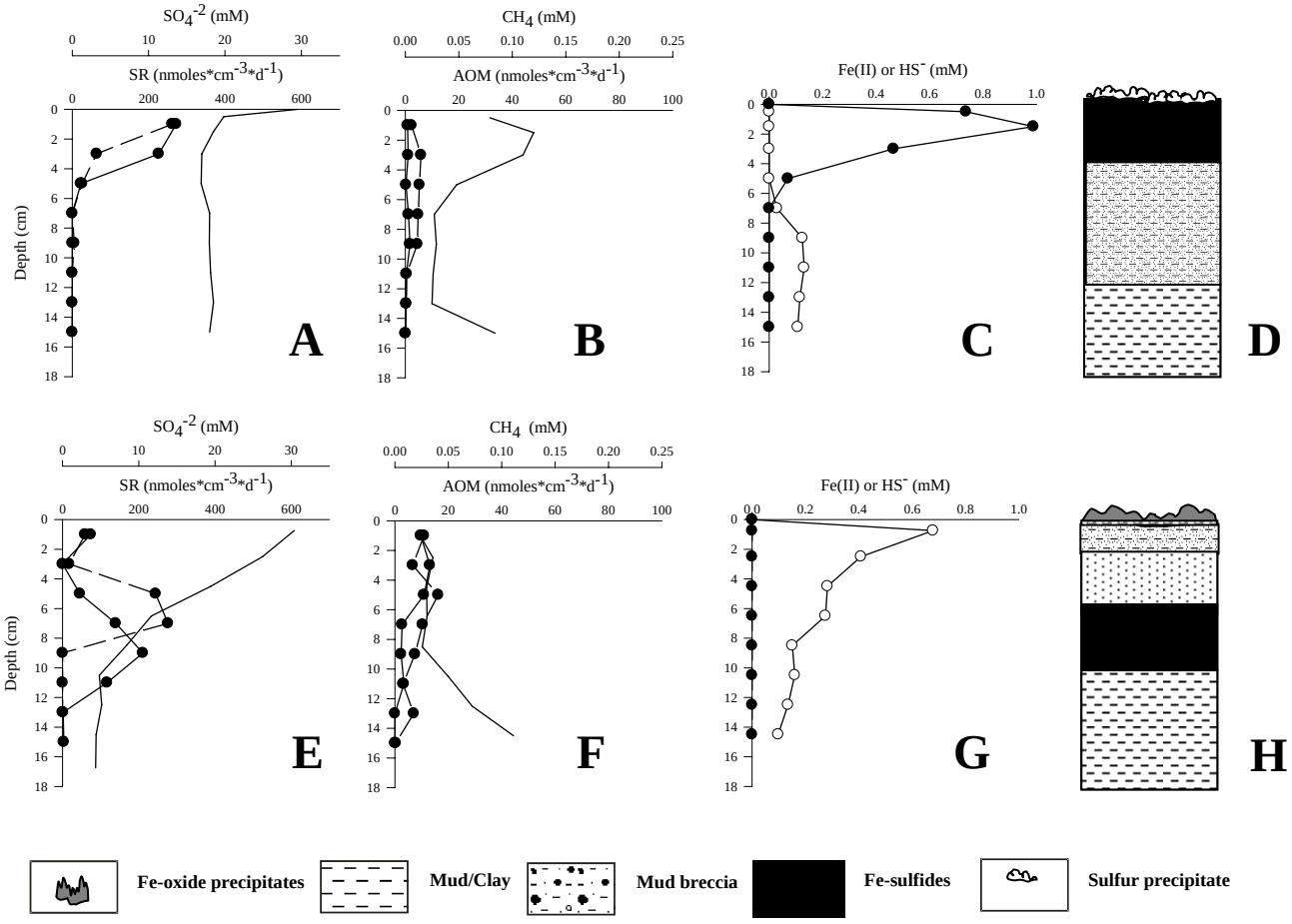
SO_4^{-2} (mM)
SR (nmoles*cm^{-3}*d^{-1})
CH_4 (mM)
AOM (nmoles*cm^{-3}*d^{-1})
Fe(II) or HS$^-$ (mM)
Depth (cm)
A
B
C
D
E
F
G
H
Fe-oxide precipitates
Mud/Clay
Mud breccia
Fe-sulfides
Sulfur precipitate

Figure 5

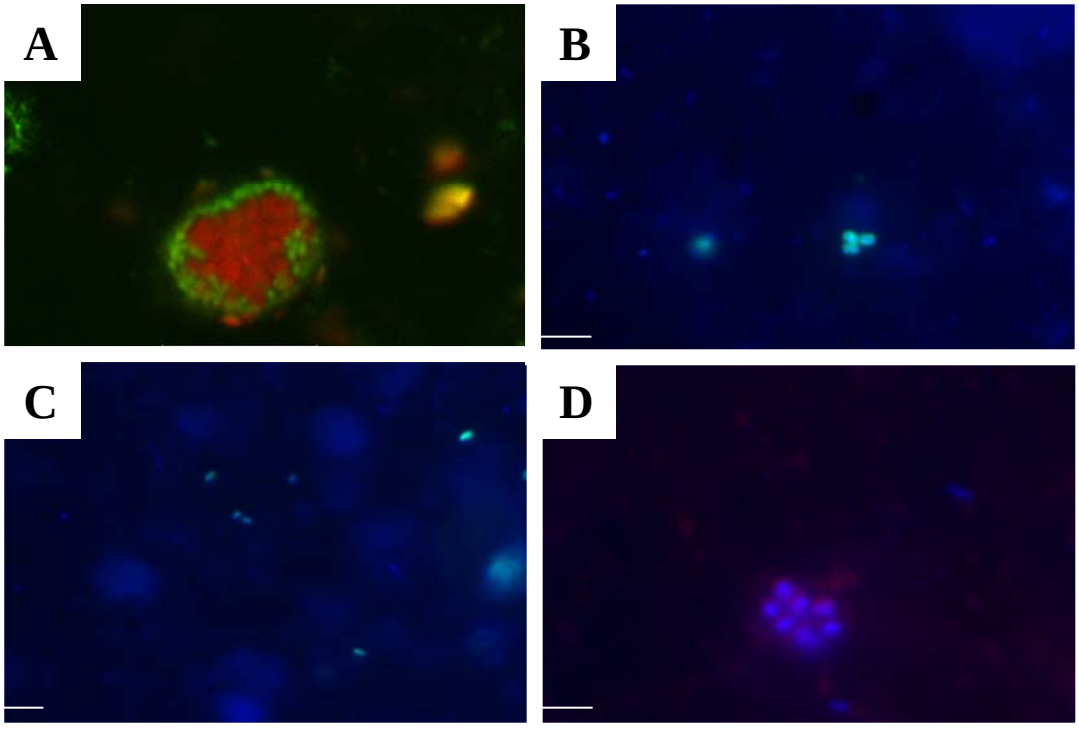

Figure 6

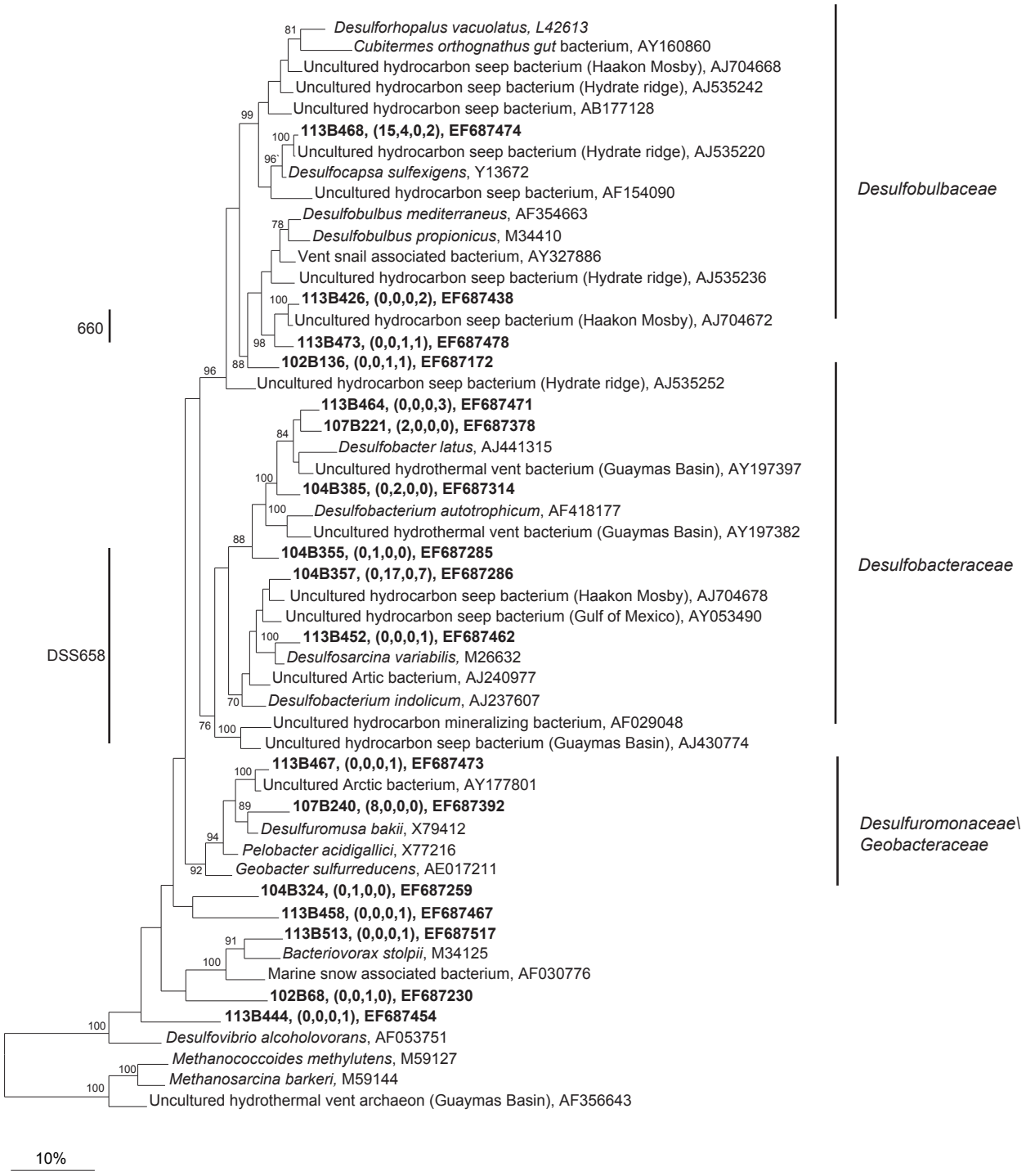
Desulforhopalus vacuolatus, L42613
Cubitermes orthognathus gut bacterium, AY160860
Uncultured hydrocarbon seep bacterium (Haakon Mosby), AJ704668
Uncultured hydrocarbon seep bacterium (Hydrate ridge), AJ535242
Uncultured hydrocarbon seep bacterium, AB177128
113B468, (15,4,0,2), EF687474
Uncultured hydrocarbon seep bacterium (Hydrate ridge), AJ535220
Desulfocapsa sulfexigens, Y13672
Uncultured hydrocarbon seep bacterium, AF154090
Desulfobulbus mediterraneus, AF354663
Desulfobulbus propionicus, M34410
Vent snail associated bacterium, AY327886
Uncultured hydrocarbon seep bacterium (Hydrate ridge), AJ535236
113B426, (0,0,0,2), EF687438
Uncultured hydrocarbon seep bacterium (Haakon Mosby), AJ704672
113B473, (0,0,1,1), EF687478
102B136, (0,0,1,1), EF687172
Uncultured hydrocarbon seep bacterium (Hydrate ridge), AJ535252
113B464, (0,0,0,3), EF687471
107B221, (2,0,0,0), EF687378
Desulfobacter latus, AJ441315
Uncultured hydrothermal vent bacterium (Guaymas Basin), AY197397
104B385, (0,2,0,0), EF687314
Desulfobacterium autotrophicum, AF418177
Uncultured hydrothermal vent bacterium (Guaymas Basin), AY197382
104B355, (0,1,0,0), EF687285
104B357, (0,17,0,7), EF687286
Uncultured hydrocarbon seep bacterium (Haakon Mosby), AJ704678
Uncultured hydrocarbon seep bacterium (Gulf of Mexico), AY053490
113B452, (0,0,0,1), EF687462
Desulfosarcina variabilis, M26632
Uncultured Artic bacterium, AJ240977
Desulfobacterium indolicum, AJ237607
Uncultured hydrocarbon mineralizing bacterium, AF029048
Uncultured hydrocarbon seep bacterium (Guaymas Basin), AJ430774
113B467, (0,0,0,1), EF687473
Uncultured Arctic bacterium, AY177801
107B240, (8,0,0,0), EF687392
Desulfuromusa bakii, X79412
Pelobacter acidigallici, X77216
Geobacter sulfurreducens, AE017211
104B324, (0,1,0,0), EF687259
113B458, (0,0,0,1), EF687467
113B513, (0,0,0,1), EF687517
Bacteriovorax stolpii, M34125
Marine snow associated bacterium, AF030776
102B68, (0,0,1,0), EF687230
113B444, (0,0,0,1), EF687454
Desulfovibrio alcoholovorans, AF053751
Methanococcoides methylutens, M59127
Methanosarcina barkeri, M59144
Uncultured hydrothermal vent archaeon (Guaymas Basin), AF356643
660
DSS658
Desulfobulbaceae
Desulfobacteraceae
Desulfuromonaceae\
Geobacteraceae
10%

Figure 7

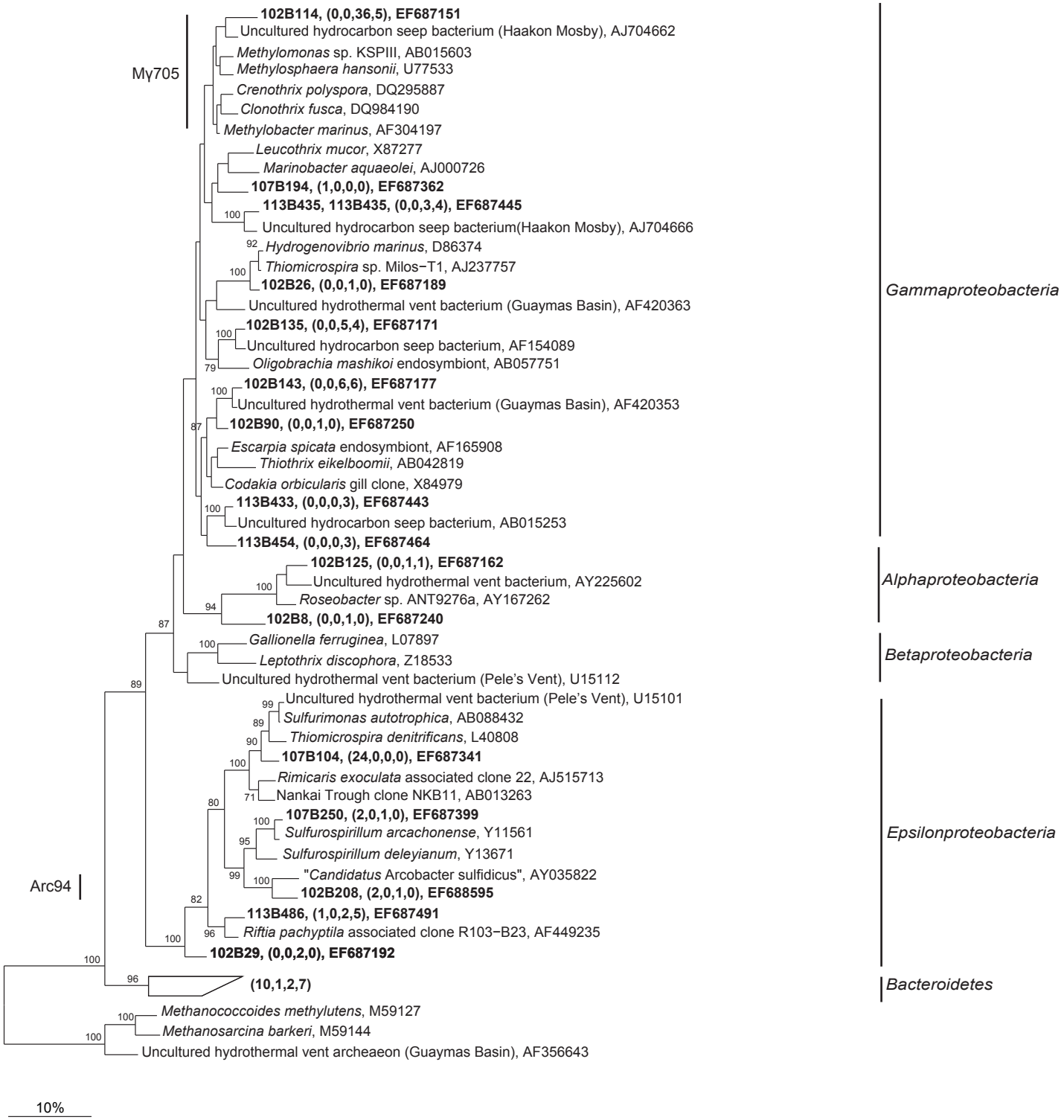
Mγ705
Arc94
102B114, (0,0,36,5), EF687151
Uncultured hydrocarbon seep bacterium (Haakon Mosby), AJ704662
Methylomonas sp. KSPIII, AB015603
Methylosphaera hansonii, U77533
Crenothrix polyspora, DQ295887
Clonothrix fusca, DQ984190
Methylobacter marinus, AF304197
Leucothrix mucor, X87277
Marinobacter aquaeolei, AJ000726
107B194, (1,0,0,0), EF687362
113B435, 113B435, (0,0,3,4), EF687445
Uncultured hydrocarbon seep bacterium(Haakon Mosby), AJ704666
Hydrogenovibrio marinus, D86374
Thiomicrospira sp. Milos−T1, AJ237757
102B26, (0,0,1,0), EF687189
Uncultured hydrothermal vent bacterium (Guaymas Basin), AF420363
102B135, (0,0,5,4), EF687171
Uncultured hydrocarbon seep bacterium, AF154089
Oligobrachia mashikoi endosymbiont, AB057751
102B143, (0,0,6,6), EF687177
Uncultured hydrothermal vent bacterium (Guaymas Basin), AF420353
102B90, (0,0,1,0), EF687250
Escarpia spicata endosymbiont, AF165908
Thiothrix eikelboomii, AB042819
Codakia orbicularis gill clone, X84979
113B433, (0,0,0,3), EF687443
Uncultured hydrocarbon seep bacterium, AB015253
113B454, (0,0,0,3), EF687464
102B125, (0,0,1,1), EF687162
Uncultured hydrothermal vent bacterium, AY225602
Roseobacter sp. ANT9276a, AY167262
102B8, (0,0,1,0), EF687240
Gallionella ferruginea, L07897
Leptothrix discophora, Z18533
Uncultured hydrothermal vent bacterium (Pele's Vent), U15112
Uncultured hydrothermal vent bacterium (Pele's Vent), U15101
Sulfurimonas autotrophica, AB088432
Thiomicrospira denitrificans, L40808
107B104, (24,0,0,0), EF687341
Rimicaris exoculata associated clone 22, AJ515713
Nankai Trough clone NKB11, AB013263
107B250, (2,0,1,0), EF687399
Sulfurospirillum arcachonense, Y11561
Sulfurospirillum deleyianum, Y13671
"Candidatus Arcobacter sulfidicus", AY035822
102B208, (2,0,1,0), EF688595
113B486, (1,0,2,5), EF687491
Riftia pachyptila associated clone R103−B23, AF449235
102B29, (0,0,2,0), EF687192
(10,1,2,7)
Methanococcoides methylutens, M59127
Methanosarcina barkeri, M59144
Uncultured hydrothermal vent archeaeon (Guaymas Basin), AF356643
Gammaproteobacteria
Alphaproteobacteria
Betaproteobacteria
Epsilonproteobacteria
Bacteroidetes
10%

Figure 8

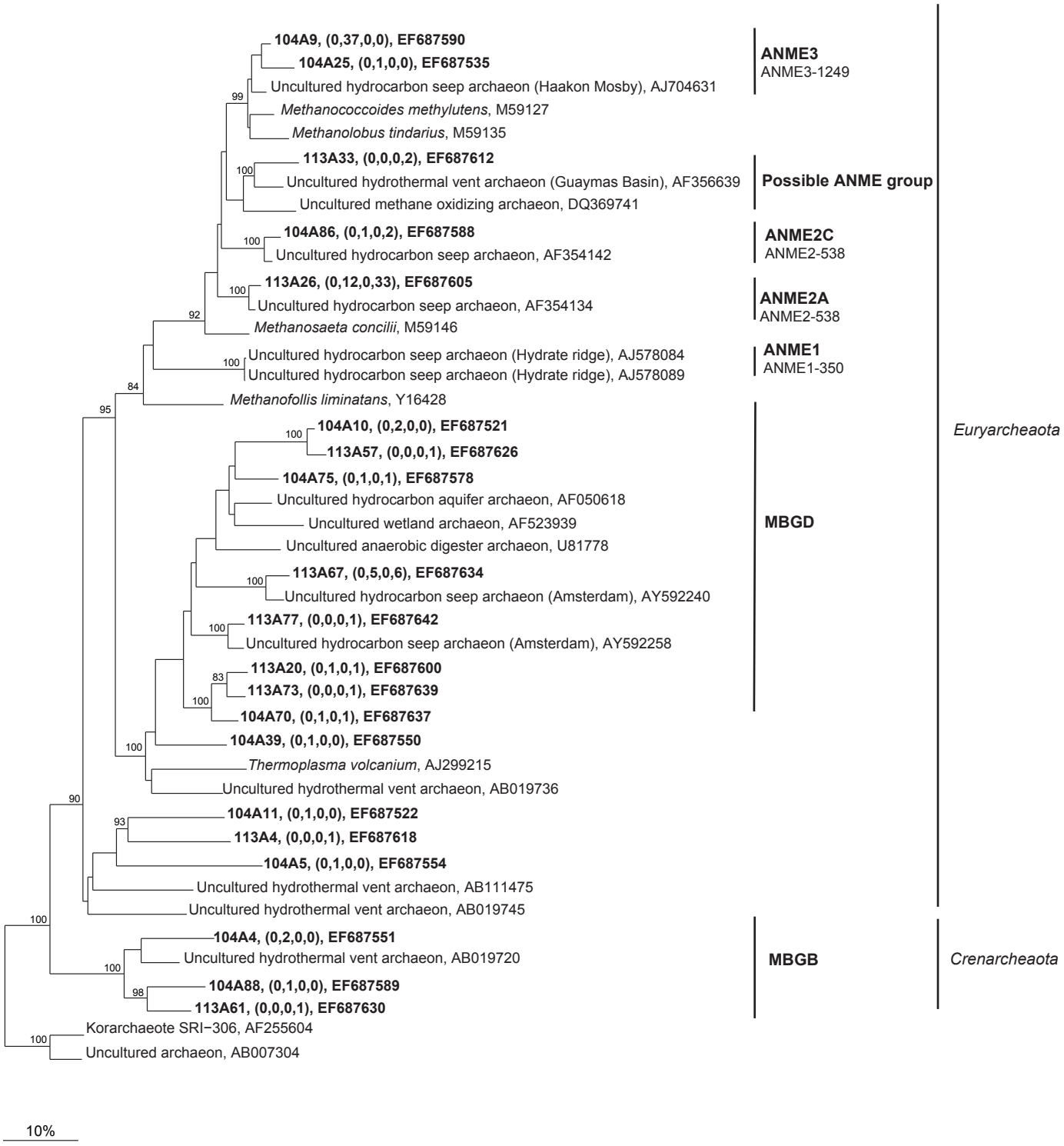
104A9, (0,37,0,0), EF687590
104A25, (0,1,0,0), EF687535
Uncultured hydrocarbon seep archaeon (Haakon Mosby), AJ704631
Methanococcoides methylutens, M59127
Methanolobus tindarius, M59135
113A33, (0,0,0,2), EF687612
Uncultured hydrothermal vent archaeon (Guaymas Basin), AF356639
Uncultured methane oxidizing archaeon, DQ369741
104A86, (0,1,0,2), EF687588
Uncultured hydrocarbon seep archaeon, AF354142
113A26, (0,12,0,33), EF687605
Uncultured hydrocarbon seep archaeon, AF354134
Methanosaeta concilii, M59146
Uncultured hydrocarbon seep archaeon (Hydrate ridge), AJ578084
Uncultured hydrocarbon seep archaeon (Hydrate ridge), AJ578089
Methanofollis liminatans, Y16428
104A10, (0,2,0,0), EF687521
113A57, (0,0,0,1), EF687626
104A75, (0,1,0,1), EF687578
Uncultured hydrocarbon aquifer archaeon, AF050618
Uncultured wetland archaeon, AF523939
Uncultured anaerobic digester archaeon, U81778
113A67, (0,5,0,6), EF687634
Uncultured hydrocarbon seep archaeon (Amsterdam), AY592240
113A77, (0,0,0,1), EF687642
Uncultured hydrocarbon seep archaeon (Amsterdam), AY592258
113A20, (0,1,0,1), EF687600
113A73, (0,0,0,1), EF687639
104A70, (0,1,0,1), EF687637
104A39, (0,1,0,0), EF687550
Thermoplasma volcanium, AJ299215
Uncultured hydrothermal vent archaeon, AB019736
104A11, (0,1,0,0), EF687522
113A4, (0,0,0,1), EF687618
104A5, (0,1,0,0), EF687554
Uncultured hydrothermal vent archaeon, AB111475
Uncultured hydrothermal vent archaeon, AB019745
104A4, (0,2,0,0), EF687551
Uncultured hydrothermal vent archaeon, AB019720
104A88, (0,1,0,0), EF687589
113A61, (0,0,0,1), EF687630
Korarchaeote SRI−306, AF255604
Uncultured archaeon, AB007304
ANME3
ANME3-1249
Possible ANME group
ANME2C
ANME2-538
ANME2A
ANME2-538
ANME1
ANME1-350
MBGD
MBGB
Euryarcheaota
Crenarcheaota
10%

Figure 9